

A comparison of the turbulent dynamo in weakly-collisional and collisional plasmas: from subsonic to supersonic turbulence

Radhika Achikanath Chirakkara,¹★ Christoph Federrath,^{1,2} and Amit Seta¹

¹Research School of Astronomy and Astrophysics, Australian National University, Canberra, ACT 2611, Australia

²Australian Research Council Centre of Excellence in All Sky Astrophysics (ASTRO3D), Canberra, ACT 2611, Australia

Accepted XXX. Received YYY; in original form ZZZ

ABSTRACT

Weakly-collisional plasmas, such as the solar wind or the intra-cluster medium (ICM) of galaxy clusters, evolve in the presence of dynamically strong magnetic fields. The turbulent dynamo can amplify magnetic fields to such levels by converting turbulent kinetic energy into magnetic energy. While extensively studied in collisional magnetohydrodynamic (MHD) simulations, the weakly-collisional regime has only been explored recently. Here, we determine the properties of the weakly-collisional turbulent dynamo in the exponential “kinematic” growth phase in both the subsonic and the previously unexplored supersonic regime of turbulence, using hybrid particle-in-cell (HPIC) and MHD simulations. We conduct a large parameter study, fixing the magnetic Reynolds number, $R_m = 500$, and the initial ratio of the magnetic to kinetic energy, $(E_{\text{mag}}/E_{\text{kin}})_0 = 10^{-10}$, and then vary the kinetic Reynolds number, $Re = 500, 50$, and 5 , for the MHD simulations. In the HPIC runs, only $R_m = 500$ is controlled, while Re emerges self-consistently from wave-particle interactions. We find that the velocity and magnetic field structures, probability distribution functions, and power spectra of the HPIC runs are similar to that of the MHD dynamo with $Re \sim 50 - 500$ and $Re \sim 500$ in the subsonic and supersonic regimes, respectively. Using MHD scaling relations, we infer $Re_{\text{inferred}} = 480^{+170}_{-250}$ and 690^{+360}_{-360} in the subsonic and supersonic weakly-collisional plasma, respectively. Overall, we find that the turbulent dynamo shares similar physical properties in both weakly-collisional and collisional plasmas. Our results of the weakly-collisional turbulent dynamo may have relevant applications to the solar wind, weakly-collisional shocks, and the hot ICM.

Key words: dynamo – turbulence – magnetic fields – methods: numerical – galaxies: clusters: intracluster medium – plasmas

1 INTRODUCTION

Plasmas can be characterised collisional or weakly-collisional based on the ratio of the mean free path, λ_{mfp} , which is the average distance that charged particles travel before interacting with another particle, and the characteristic system size, L . The system is considered collisional if the mean free path is much smaller than the system size, as is the case in the interstellar medium, where $\lambda_{\text{mfp}}/L \ll 1$ from the hot ionised medium to the cold molecular phase (Ferrière 2020). Such plasmas have been conventionally studied using collisional magnetohydrodynamical (MHD) simulations. However, for many plasmas such as the hot intracluster medium (hot ICM) of galaxy clusters, $\lambda_{\text{mfp}}/L \sim 0.1 - 1$, making this plasma weakly-collisional (Schekochihin & Cowley 2006). In this weakly-collisional regime, the MHD equations are inadequate for modelling the plasma, and we have to resort to kinetic methods. This is also true for the solar wind, cosmic-ray acceleration, and any scenario involving collisionless shocks, kinetic instabilities, and magnetic reconnection (Kulsrud 2005). This study aims to understand the amplification of magnetic fields in such weakly-collisional turbulent plasmas, particularly in the previously unexplored compressible and supersonic regime, and to contrast it with the well-studied MHD regime. Compressibility is relevant for many of these systems, and here we consider the ICM

of galaxy clusters as a specific example of a compressible weakly-collisional plasma (Hoang et al. 2017).

The hot ICM has extremely high temperatures of $\approx 10^7 - 10^8$ K, and is very diffuse with particle number densities of $\approx 10^{-3} \text{ cm}^{-3}$ (Simionescu et al. 2019; Kunz et al. 2022). Dynamically strong magnetic fields have been observed in the hot ICM with $\sim \mu\text{G}$ strength up to Mpc scales (Bonafede et al. 2010, 2013; Botteon et al. 2022). From gamma-ray observations of TeV blazars, a lower limit on the magnetic field strength of $\sim 10^{-12} - 10^{-10} \mu\text{G}$ in the voids of the large-scale structure of the Universe has been inferred (Neronov & Vovk 2010; Tavecchio et al. 2010; Taylor et al. 2011; Vovk et al. 2012; Finke et al. 2015; Ackermann et al. 2018). These magnetic fields, which can be of astrophysical or primordial origin, are much smaller than the μG magnetic fields observed in the hot ICM. Thus, there must be a powerful amplification mechanism to explain the fields observed today: the turbulent dynamo, which is the process of converting the kinetic energy of turbulence to magnetic energy (Kazantsev 1968; Moffatt 1978; Brandenburg & Subramanian 2005).

However, the turbulent dynamo process requires sustained turbulence. Galaxy mergers, wakes of infalling galaxies, and AGN can indeed drive the required turbulence in the hot ICM of galaxy clusters (Simionescu et al. 2019). Turbulent motions $\approx 160 \text{ km s}^{-1}$ have been observed in the Perseus cluster by the Hitomi collaboration (Hitomi Collaboration et al. 2016). Recent X-ray spectroscopy studies have inferred subsonic Mach numbers, $\mathcal{M} \sim 0.2 - 0.4$ in galaxy clusters,

★ E-mail: radhika.achikanathchirakkara@anu.edu.au

reaching transonic levels ($M \sim 1$) close to the cluster centres (Gatuzz et al. 2022a,b, 2023). Additionally, high-fidelity radio observations reveal supersonic Mach numbers, $M \sim 2.5$, in shocked regions of the sausage relic (Hoang et al. 2017). Thus, subsonic, incompressible theories and simulations (Rincon et al. 2016; St-Onge & Kunz 2018; Achikanath Chirakkara et al. 2024a) are likely insufficient to explain the dynamo amplification in these cosmic structures.

The turbulent dynamo, broadly, has three stages. First, a kinematic regime (1), where the weak seed magnetic field grows exponentially on small length scales; then a transition regime (2), where the magnetic field grows in a power-law fashion, often described as linear for subsonic flows (Cho et al. 2009; Xu & Lazarian 2016; Seta & Federrath 2020; Beattie et al. 2023), and the coherence length scale of the magnetic field increases; and finally, a saturation phase (3), where the fields cease growing, but are still maintained by the dynamo. The turbulent dynamo has been widely studied using collisional MHD simulations (Schekochihin et al. 2004; Haugen et al. 2004; Federrath et al. 2014; Federrath 2016; Seta et al. 2020; Seta & Federrath 2020, 2021a,b, 2022; Kriel et al. 2022; Gent et al. 2023), and its role in amplifying weak seed magnetic fields to strong dynamical levels have been explored in many astrophysical environments including star-forming molecular clouds (Sur et al. 2010; Federrath et al. 2011b), young galaxies (Schober et al. 2013), and galaxy clusters (Subramanian et al. 2006; Bhat & Subramanian 2013; Vazza et al. 2018; Sur 2019). Properties of the MHD turbulent dynamo, like the growth rate of magnetic energy and the saturation efficiency, depend on the Mach number of the plasma and the nature of the turbulent driving (Federrath et al. 2011a; Achikanath Chirakkara et al. 2021). Recent laboratory experiments have also demonstrated the turbulent dynamo mechanism in different Mach number regimes (Tzeferacos et al. 2017, 2018; Chen et al. 2020; Bott et al. 2021a,b), confirmed in simulations (Hu et al. 2022; Hew & Federrath 2023). The plasmas in the above numerical studies and experiments are collisional (e.g. $\lambda_{\text{mfp}}/L \sim 10^{-3}$, see Tzeferacos et al. 2018).

The possibility of a turbulent dynamo in weakly-collisional plasmas has only recently been explored, with several approaches employed to study the weakly-collisional turbulent dynamo (Rincon et al. 2016; St-Onge & Kunz 2018; St-Onge et al. 2020; Achikanath Chirakkara et al. 2024a,b; Sironi et al. 2023; Zhou et al. 2024). For example, Sironi et al. (2023) and Zhou et al. (2024) use the fully kinetic particle-in-cell (PIC) approach, which models all plasma components, including ions and electrons, as particles. This makes the approach computationally demanding. In the hybrid-kinetic approach, ions are modelled kinetically, while electrons are treated as a fluid. St-Onge & Kunz (2018) and Achikanath Chirakkara et al. (2024a) use the hybrid particle-in-cell (hybrid PIC) approach, where Lagrangian particles sample the moments of the ion distribution function, while electrons are described as a fluid. The hybrid PIC approach is computationally less expensive and can be used to study the system on ion length- and time-scales, which are much larger than the electron length- and time-scales. Therefore, we use the hybrid PIC approach in the present work.

The properties of the weakly-collisional turbulent dynamo for different parameter regimes, especially in the supersonic regime, are still unknown. Furthermore, it is not clear how the properties of the weakly-collisional turbulent dynamo compare to those of its well-studied collisional MHD counterpart. In this paper, we study the weakly-collisional turbulent dynamo using hybrid PIC simulations in the subsonic and the previously unexplored supersonic regime and compare it with the MHD turbulent dynamo.

Unlike in MHD, where viscosity is a parameter that can be set in numerical simulations, the effective viscosity of a weakly-collisional

plasma is determined self-consistently by wave-particle interactions (Schekochihin & Cowley 2006). This makes it challenging to ascertain the kinetic Reynolds number, viscous dissipation scale, and magnetic Prandtl number – all critical plasma parameters for studying the turbulent dynamo in weakly-collisional plasmas. In this work, we address this by applying viscous and magnetic scaling relations from studies of the MHD turbulent dynamo to the weakly-collisional regime.

The rest of this work is organised in the following way. We describe the hybrid-kinetic and MHD equations, the numerical methods, and the initial conditions and parameters for the turbulent dynamo simulations in Sec. 2. In Sec. 3, we discuss the morphology, time evolution, probability density functions, and the power spectra for the weakly-collisional and the collisional MHD turbulent dynamo in the subsonic and the supersonic regime. The kinetic Reynolds number and the turbulent dissipation scale of the weakly-collisional turbulent dynamo simulations are estimated using MHD scaling relations in Sec. 4. Finally, we conclude our study in Sec. 5.

2 METHODS

We use the hybrid PIC method (henceforth referred to as HPIC) AHKASH (Achikanath Chirakkara et al. 2024b) to perform numerical experiments of the weakly-collisional dynamo, while the collisional MHD simulations presented in this study are performed with the HLL5R Riemann scheme (Waagan et al. 2011). Both HPIC and MHD methods used here are implemented in the FLASH code framework (Fryxell et al. 2000; Dubey et al. 2008a,b).

2.1 Hybrid-kinetic equations

For the simulations of weakly-collisional plasmas, we solve the hybrid-kinetic equations (written here in SI units) using the HPIC method. In the HPIC approach, the positively charged ions are treated as particles, and the positions and velocities of the particles are evolved using the equations of motion,

$$\frac{d\mathbf{r}_p}{dt} = \mathbf{v}_p, \quad (1)$$

$$\frac{d\mathbf{v}_p}{dt} = \frac{q_i}{m_i} (\mathbf{E} + \mathbf{v}_p \times \mathbf{B}) + \mathbf{f}, \quad (2)$$

where \mathbf{r}_p and \mathbf{v}_p are the position and velocity of the p^{th} particle, respectively, with $p = 1, 2, \dots, P$, where P is the total number of particles. The quantities q_i and m_i are the ion charge and mass, respectively. The ions (particles) move under the influence of the electric (\mathbf{E}) and magnetic (\mathbf{B}) fields and sample the moments of the ion distribution function. The additional turbulent acceleration field, \mathbf{f} , further described in Sec. 2.4, is used to drive turbulence in the plasma.

The electrons are treated as a massless fluid in the hybrid-kinetic approach. The electric field is calculated using the following Ohm's law (Rosin et al. 2011),

$$\mathbf{E} = \frac{(\mathbf{J} - \mathbf{J}_i) \times \mathbf{B}}{\rho_i} - \frac{\nabla p_e}{\rho_i} + \mu_0 \eta \mathbf{J} - \mu_0 \eta_{\text{hyper}} \nabla^2 \mathbf{J}, \quad (3)$$

where $\mathbf{J} = (\nabla \times \mathbf{B})/\mu_0$ is the total current, i.e., the sum of the ion and electron currents. The charge density, ρ_i , and ion current, \mathbf{J}_i , are sampled from the particles. The electron pressure, p_e , is modelled using the ideal gas equation of state, $p_e = n_e k_B T_e$, where n_e , T_e , and k_B are the electron number density, electron temperature, and the Boltzmann constant, respectively. We assume the electrons

are isothermal ($T_e = \text{constant}$). We also assume that the plasma is quasi-neutral, $\rho_e = -\rho_i$, where ρ_e is the electron charge density, μ_0 is the magnetic permeability constant. The diffusivity, η , sets the Ohmic dissipation of the plasma. The final term on the right-hand side of Eq. 3 is the numerical hyper-resistivity, and η_{hyper} is the hyper-diffusivity co-efficient, which is used to suppress numerical fluctuations near the grid scale.

The magnetic field is computed using Faraday's law,

$$\frac{\partial \mathbf{B}}{\partial t} = -\nabla \times \mathbf{E}, \quad (4)$$

solved using the constrained transport method, which ensures that the magnetic fields are divergence-free ($\nabla \cdot \mathbf{B} = 0$). We use the cloud-in-cell kernel to perform interpolation operations between the particles and the computational grid to compute moments of the ion distribution. We perform a smoothing operation on the moments sampled from particles, to reduce particle noise due to limited sampling of the ion distribution function (e.g. see Fig. 12 in Achikanath Chirakkara et al. (2024b) for further details). The hybrid PIC simulations in this work are done using the AHKASH code, which is described in detail with relevant tests in Achikanath Chirakkara et al. (2024b).

2.2 Cooling for hybrid particle-in-cell simulations

Various physical processes can act to heat and cool a plasma. A balance between heating and cooling leads to a constant plasma temperature, and thus a constant thermal speed of the ions in many physical systems. Therefore, it is often desirable to model a plasma with constant temperature. In hybrid PIC, one can directly set an isothermal equation of state for the electrons, as discussed in Sec. 2.1. However, this approach is not applicable to ions, which are treated as particles. Therefore, a cooling method is necessary to keep the ions isothermal and ensure they maintain the same temperature as the electrons. Without a cooling method, various heating sources, such as turbulence or shock dissipation, make it impossible to achieve steady-state turbulence with a time-independent root mean square (rms) Mach number.

To mitigate this issue, we have introduced a cooling method based on locally rescaling the ion thermal speed, u_{th} (Sec. 2.11 and Sec. 5 in Achikanath Chirakkara et al. 2024b, for the description of the method and related tests). This cooling method maintains isothermal conditions locally and globally throughout the computational domain and in time. In the subsonic regime, cooling is performed on a cooling timescale, $(\Delta t)_{\text{cool}} = 0.1 t_{\text{cool}}$ and $t_{\text{cool}} = t_{\text{th}}/\mathcal{M}$, where $t_{\text{th}} = \Delta l/u_{\text{th}}$ is the thermal crossing time (the time taken by sound waves to travel across a grid cell of size Δl) and \mathcal{M} is the Mach number of the plasma. In the supersonic regime, a shorter cooling timescale, $(\Delta t)_{\text{cool}} = 0.01 t_{\text{cool}}$, is required as more energy compared to the thermal energy is injected into the plasma in the supersonic case and dissipative shocks are present.

2.3 Magnetohydrodynamic equations

For the MHD simulations, we use the HLL5R Riemann scheme (Bouchut et al. 2007, 2010; Waagan et al. 2011), solving the isother-

mal compressible MHD equations (written in CGS units),

$$\frac{\partial \rho}{\partial t} + \nabla \cdot (\rho \mathbf{u}) = 0, \quad (5)$$

$$\frac{\partial (\rho \mathbf{u})}{\partial t} + \nabla \cdot (\rho \mathbf{u} \otimes \mathbf{u} - \mathbf{B} \otimes \mathbf{B}) = -\nabla p + \nabla \cdot (2\nu \rho \mathbf{S}) + \rho \mathbf{f}, \quad (6)$$

$$\frac{\partial \mathbf{B}}{\partial t} = \nabla \times (\mathbf{u} \times \mathbf{B}) + \eta \nabla^2 \mathbf{B}, \quad (7)$$

$$\nabla \cdot \mathbf{B} = 0, \quad (8)$$

where ρ is the mass density of the gas, \mathbf{u} is the velocity, \mathbf{B} is the magnetic field, p is the pressure, which includes both the thermal pressure, p_{th} and the magnetic pressure, $p_{\text{mag}} = B^2/(8\pi)$, and \mathbf{f} is the turbulent acceleration field, same as used in Sec. 2. The viscosity and Ohmic diffusivity are denoted by ν and η , respectively. The rate of strain tensor, S_{ij} , is given by $S_{ij} = 1/2(\partial_i u_j + \partial_j u_i - (2/3)\delta_{ij} \nabla \cdot \mathbf{u})$. The MHD equations are closed with an isothermal equation of state, $p_{\text{th}} = \rho u_{\text{th}}^2$, with a constant sound speed c_s . So, the energy equation of MHD does not need to be solved. We set the viscosity and diffusivity such that specific target Reynolds numbers are achieved given the available numerical resolution (Malvadi Shivakumar & Federrath 2023) in our numerical experiments (detailed in Sec. 2.5).

2.4 Turbulent driving

The turbulent driving field, \mathbf{f} , is modelled using the Ornstein–Uhlenbeck process using the turbulence generator TurbGen (Federrath et al. 2010, 2022) for both the HPIC and MHD cases. Turbulence is driven on large scales, i.e., wave numbers satisfying $kL/2\pi = (1, 3)$, where L is the side length of the cubic computational domain. The driving amplitude is controlled by a parabolic function that peaks at $k_{\text{turb}}L/2\pi = 2$, and falls to zero at $kL/2\pi = 1, 3$. In this study, we focus on purely solenoidal driving ($\nabla \cdot \mathbf{f} = 0$), which injects solenoidal acceleration modes into the plasma with exactly the same f for the HPIC and MHD simulations.

2.5 Plasma parameters and initial conditions

This section discusses the important parameters and initial conditions of our HPIC and MHD turbulent dynamo numerical simulations. We perform the HPIC simulations on a periodic computational box with $N_{\text{grid}}^3 = 128^3$ grid cells and $N_{\text{ppc}} = 100$ particles per cell. We also test and demonstrate numerical convergence by varying the grid resolution, $N_{\text{grid}}^3 = 64^3$ and 256^3 , and the particle resolution, $N_{\text{ppc}} = 50$ and 200 in Appendix A. For a better comparison, the MHD simulations are also performed on $N_{\text{grid}}^3 = 128^3$ grid cells with periodic boundary conditions. To demonstrate the convergence of the MHD simulations, we vary the grid resolution, $N_{\text{grid}}^3 = 64^3$ and 256^3 in Appendix B.

2.5.1 Plasma parameters

First, the plasma parameters that are important for the turbulent dynamo problem are discussed. The Mach number, \mathcal{M} , quantifies the compressibility of the plasma and is defined as

$$\mathcal{M} = \frac{u_{\text{turb}}}{u_{\text{th}}}, \quad (9)$$

where u_{turb} is the turbulent speed and u_{th} is the thermal speed. We study the turbulent dynamo in subsonic and supersonic regimes with $\mathcal{M} = 0.2$ and $\mathcal{M} = 2$, respectively. We fix the thermal speed while varying the turbulent speed to achieve different Mach numbers. The

Table 1. List of simulations with the corresponding model name, grid resolution (N_{grid}^3), particle-per-cell count (N_{ppc}), Mach number (\mathcal{M}), initial magnetic to kinetic energy ratio ($(E_{\text{mag}}/E_{\text{kin}})_0$), initial plasma beta (β_0), initial Larmor ratio ($(r_{\text{Larmor}}/L)_0$), magnetic Reynolds number (Rm), kinetic Reynolds number (Re), magnetic Prandtl number (Pm), dynamo growth rate of the magnetic energy (Γ), and the magnetic dissipation scale (k_η).

Ser. No	Model	N_{grid}^3	N_{ppc}	\mathcal{M}	$(E_{\text{mag}}/E_{\text{kin}})_0$	β_0	$(r_{\text{Larmor}}/L)_0$	Rm	Re	Pm	$\Gamma (t_0^{-1})$	k_η
1	HPICM0.2Rm500	128 ³	100	0.20±0.02	10 ⁻¹⁰	5 × 10 ¹¹	10 ²	502±41	–	–	0.49±0.05	9.5±1.0
2	MHDM0.2Rm500Re500	128 ³	–	0.20±0.01	10 ⁻¹⁰	5 × 10 ¹¹	–	500±26	500±26	1	0.38±0.02	10.8±1.0
3	MHDM0.2Rm500Re50	128 ³	–	0.20±0.01	10 ⁻¹⁰	5 × 10 ¹¹	–	504±35	50.4±3.5	10	0.55±0.01	8.4±1.0
4	MHDM0.2Rm500Re5	128 ³	–	0.20±0.02	10 ⁻¹⁰	5 × 10 ¹¹	–	500±40	5.0±0.4	100	0.54±0.03	7.2±1.0
5	HPICM2Rm500	128 ³	100	1.91±0.12	10 ⁻¹⁰	5 × 10 ⁹	10 ²	476±30	–	–	0.37±0.05	9.9±1.1
6	MHDM2Rm500Re500	128 ³	–	1.95±0.09	10 ⁻¹⁰	5 × 10 ⁹	–	488±23	488±23	1	0.14±0.05	9.3±1.0
7	MHDM2Rm500Re50	128 ³	–	1.99±0.10	10 ⁻¹⁰	5 × 10 ⁹	–	497±25	49.7±2.5	10	0.44±0.03	8.1±1.0
8	MHDM2Rm500Re5	128 ³	–	1.92±0.14	10 ⁻¹⁰	5 × 10 ⁹	–	479±36	4.8±0.4	100	0.55±0.04	7.1±1.0
9	HPICM0.2Rm500Nppc50	128 ³	50	0.20±0.02	10 ⁻¹⁰	5 × 10 ¹¹	10 ²	501±42	–	–	0.51±0.04	9.5±1.1
10	HPICM0.2Rm500Nppc200	128 ³	200	0.20±0.02	10 ⁻¹⁰	5 × 10 ¹¹	10 ²	503±41	–	–	0.47±0.06	9.5±1.0
11	HPICM2Rm500Nppc50	128 ³	50	1.91±0.11	10 ⁻¹⁰	5 × 10 ⁹	10 ²	478±27	–	–	0.41±0.01	10.1±1.1
12	HPICM2Rm500Nppc200	128 ³	200	1.92±0.11	10 ⁻¹⁰	5 × 10 ⁹	10 ²	479±28	–	–	0.39±0.01	10.0±1.2
13	HPICM0.2Rm500Ngrid64	64 ³	100	0.20±0.02	10 ⁻¹⁰	5 × 10 ¹¹	10 ²	499±46	–	–	0.56±0.02	8.9±1.0
14	HPICM0.2Rm500Ngrid256	256 ³	100	0.20±0.02	10 ⁻¹⁰	5 × 10 ¹¹	10 ²	500±40	–	–	0.48±0.06	9.4±1.0
15	HPICM2Rm500Ngrid64	64 ³	100	1.85±0.10	10 ⁻¹⁰	5 × 10 ⁹	10 ²	463±26	–	–	0.44±0.05	8.8±1.0
16	HPICM2Rm500Ngrid256	256 ³	100	1.98±0.12	10 ⁻¹⁰	5 × 10 ⁹	10 ²	494±29	–	–	0.46±0.05	10.7±1.4
17	MHDM0.2Rm500Re500Ngrid64	64 ³	–	0.20±0.01	10 ⁻¹⁰	5 × 10 ¹¹	–	500±26	500±26	1	0.43±0.02	7.7±1.0
18	MHDM0.2Rm500Re500Ngrid256	256 ³	–	0.20±0.01	10 ⁻¹⁰	5 × 10 ¹¹	–	503±34	503±34	1	0.45±0.02	12.6±1.0
19	MHDM2Rm500Re500Ngrid64	64 ³	–	1.93±0.09	10 ⁻¹⁰	5 × 10 ⁹	–	483±22	483±22	1	0.06±0.01	11.2±5.2
20	MHDM2Rm500Re500Ngrid256	256 ³	–	1.96±0.09	10 ⁻¹⁰	5 × 10 ⁹	–	489±22	489±22	1	0.16±0.04	11.1±1.0

turbulent crossing time, $t_0 = L_{\text{turb}}/u_{\text{turb}}$, where $L_{\text{turb}} = L/2$. The magnetic Reynolds number is defined as

$$\text{Rm} = \frac{u_{\text{turb}} L_{\text{turb}}}{\eta}, \quad (10)$$

where η is the Ohmic diffusivity. We set $\text{Rm} \approx 500$ in all our simulations, which is resolvable with a grid resolution of $N_{\text{grid}}^3 = 128^3$ in both the subsonic and supersonic regime (See Fig. 8 of [Malvadi Shivakumar & Federrath \(2023\)](#)). We also use numerical hyper-resistivity in the HPIC simulations to remove grid-scale fluctuations in the magnetic field. The hyper-resistive Reynolds number is defined as

$$\text{Rm}_{\text{hyper}} = \frac{u_{\text{turb}} L_{\text{turb}}^3}{\eta_{\text{hyper}}}. \quad (11)$$

We set $\text{Rm}_{\text{hyper}} = N_{\text{grid}}^{10/3}$ for the HPIC simulations, where N_{grid} is the grid resolution (Sec. 2.5.2 of [Achikanath Chirakkara et al. \(2024a\)](#)). For the MHD simulations, we set the kinetic Reynolds number,

$$\text{Re} = \frac{u_{\text{turb}} L_{\text{turb}}}{\nu}, \quad (12)$$

to $\text{Re} = 500, 50$, and 5 in different simulations, where ν is the kinematic viscosity. The simulations with $\text{Re} = 50$ and $\text{Re} = 5$ are highly viscous and not turbulent. While Re is controlled directly in the MHD simulations, in HPIC, the viscosity of the plasma arises self-consistently from wave-particle interactions.

The magnetic Prandtl number is defined as

$$\text{Pm} = \frac{\text{Rm}}{\text{Re}}. \quad (13)$$

Changing Re in the MHD simulations varies $\text{Pm} = 1, 10$ and 100 for $\text{Re} = 500, 50$ and 5 , respectively. The Re and, consequently, the Pm of the weakly-collisional turbulent dynamo cannot be set as for the MHD simulations and we aim to infer the self-consistently developed Re and Pm from our HPIC simulations.

2.5.2 Initial conditions

Here, we discuss the initial conditions for the turbulent dynamo simulations. The initial magnetic to turbulent kinetic energy ratio, $(E_{\text{mag}}/E_{\text{kin}})_0$, can be re-written in the form of the initial plasma beta, β_0 , and the Mach number, as

$$(E_{\text{mag}}/E_{\text{kin}})_0 = \frac{2}{\beta_0 \mathcal{M}^2}, \quad (14)$$

where plasma β is the ratio of thermal to magnetic pressure. An initial uniform magnetic field is set up for both the HPIC and MHD runs. We set $(E_{\text{mag}}/E_{\text{kin}})_0 = 10^{-10}$ in all simulations to initialise an extremely weak magnetic field that can be amplified by the turbulent dynamo.

The Larmor ratio, defined as the ratio of the Larmor radius to the simulation box size, is an important parameter for studying the weakly-collisional turbulent dynamo and quantifies the magnetisation level of the plasma ([Achikanath Chirakkara et al. 2024a](#)). The initial Larmor ratio is

$$(r_{\text{Larmor}}/L)_0 = \frac{m_i u_{\text{th}}}{q_i b_0 L}, \quad (15)$$

where b_0 is the initial magnetic field strength. We set $(r_{\text{Larmor}}/L)_0 = 100$ in the HPIC simulations. [Achikanath Chirakkara et al. \(2024a, sec 2.5\)](#) provide further details on the initial conditions used here, in particular on how they relate various plasma parameters. The HPIC simulations are performed using the hybrid-precision method, which significantly reduces the computational cost of these runs ([Federrath et al. 2021; Achikanath Chirakkara et al. 2024b](#)).

2.5.3 Simulation table

For all simulations presented in this work, we tabulate the grid and particle resolutions, initial conditions, the magnetic and kinetic

Reynolds numbers, the magnetic Prandtl number, the measured dynamo growth rate, and the magnetic energy dissipation scale in Tab. 1.

3 RESULTS

In this section, we discuss the weakly-collisional HPIC and collisional MHD turbulent dynamo in both the subsonic and supersonic regimes. First, we study the density, velocity, and magnetic field structures in Sec. 3.1. The time evolution and growth rate of the dynamo in the kinematic regime are discussed in Sec. 3.2. The probability density functions of the density, velocity, and magnetic field are studied in Sec. 3.3. Finally, we discuss the power spectra of the magnetic energy, current, and turbulent kinetic energy in Sec. 3.4.

3.1 Density, velocity, and magnetic structures

Fig. 1 shows slice plots of density, velocity, and magnetic field for our HPIC and MHD simulations in the subsonic regime with $\mathcal{M} = 0.2$ in the middle of the kinematic regime ($t = 10 t_0$). The magnetic energy grows exponentially in the kinematic regime of the turbulent dynamo ($t = 3 - 17 t_0$), which is discussed further in Sec. 3.2.

The first column shows that the density fluctuations are overall small with $\lesssim 10\%$ as expected for subsonic plasmas. The HPIC run shows some indication of particle noise ($\lesssim 10\%$), as expected (Achikanath Chirakkara et al. 2024b). For the MHD simulations, we see that the density fluctuations decrease with decreasing Re due to the increased smoothing of velocity fluctuations with increasing viscosity.

The second column of Fig. 1 shows that large-scale velocity structures are present in all runs, due to the driving modes being primarily on large scales (c.f., Sec. 2.4). Similar to the smoothing of density fluctuations, we see that smaller-scale velocity fluctuations decrease as Re decreases in the MHD simulations. For Re = 5, we find that the velocity structures primarily exist on the driving scale. The velocity structure of HPIC resembles that of the Re = 50 – 500 MHD runs.

The third column of Fig. 1 shows the magnetic field structure. We find small-scale magnetic field fluctuations in HPIC, visually similar to the MHD runs with Re = 500 and Re = 50. For the Re = 5 MHD run, small-scale structures in the magnetic field are absent, and only large-scale fluctuations near the driving scale remain. Comparing HPIC and MHD in the subsonic regime, the closest visual resemblance is between HPIC and the Re $\sim 50 - 500$ MHD runs.

Fig. 2 shows the corresponding slice plots in the supersonic regime ($\mathcal{M} = 2$). The biggest difference compared to the subsonic regime are the strong density fluctuations and the emergence of shocks and large-scale filamentary structure here, as well as the fact that the density and velocity structures have significant correlations, which has been found in previous works on supersonic turbulence (Padoan et al. 1997; Kowal et al. 2007; Kritsuk et al. 2007; Federrath et al. 2010). Visually, the supersonic HPIC run is also structurally most similar to the MHD run with Re $\sim 50 - 500$.

3.2 Time evolution

Here we discuss the time evolution of the Mach number (\mathcal{M}) and the magnetic energy (E_m/E_{m0}). The left and right panels of Fig. 3 show the subsonic ($\mathcal{M} = 0.2$) and supersonic ($\mathcal{M} = 2$) runs, respectively, with the top panels showing \mathcal{M} and the bottom panels showing E_m/E_{m0} . All runs reach the target steady-state Mach number after a short initial transient phase ($t/t_0 \sim 0 - 3$).

The magnetic energy (bottom panels) shows an exponential

growth, characteristic of the turbulent dynamo in the kinematic phase. We fit an exponential function, $E_m \propto e^{\Gamma t}$, in $t/t_0 = 3 - 17$ to determine the growth rate Γ in each model. The uncertainties in Γ are calculated as described in Appendix C of Achikanath Chirakkara et al. (2024a), with all fitted values reported in Tab. 1. As the magnetic Prandtl number of the MHD runs increases, Γ increases in both the subsonic and supersonic regimes. The growth rate of the HPIC simulation is similar to that of the Re = 5 – 500 MHD runs ($\text{Pm} = 1 - 100$) in the subsonic regime, whereas in the supersonic regime, it resembles that of the Re = 50 – 500 MHD runs ($\text{Pm} = 1 - 10$). Numerical resolution tests for the growth rate are provided in Appendix A and Appendix B, confirming that the Γ values reported here are converged.

3.3 Probability density function

In this section, we study the probability density functions (PDFs) of the density, velocity, and magnetic field.

3.3.1 Density PDF

First, we study the density PDFs of the HPIC and MHD simulations in the subsonic and supersonic regimes. Fig. 4 shows the PDFs of the natural logarithm of mass density, ρ , normalised to the mean mass density, $\langle \rho \rangle$, time-averaged in the kinematic phase of the dynamo (within time range, $3 \leq t/t_0 \leq 17$). The data points in all the PDFs shown henceforth represent the median of the time-averaged data, and the lower and upper error bars show the 16th and 84th percentile, respectively. The $\mathcal{M} = 0.2$ and 2 simulations are shown by the left and right panels, respectively.

All density PDFs are consistent with Gaussian functions in $\ln(\rho)$ (log-normal in ρ), as expected for turbulent flows (Vázquez-Semadeni 1994; Padoan et al. 1997; Passot & Vázquez-Semadeni 1998; Kritsuk et al. 2007; Federrath et al. 2008; Konstandin et al. 2012). The more viscous MHD runs (i.e., the runs with lower Re) show narrower distributions, which reflects the suppression of density fluctuations in highly viscous plasmas. The density fluctuations are substantially larger (by orders of magnitude) in $\mathcal{M} = 2$ compared to $\mathcal{M} = 0.2$ due to the development of shocks in the supersonic regime. The density fluctuations in the supersonic HPIC run agree with those in the respective Re = 50 – 500 MHD runs. In contrast, the subsonic HPIC run has a somewhat larger dispersion compared to the respective MHD runs, due to PIC noise dominating the density fluctuations in the subsonic regime, as we saw in the density slices (c.f. top left panel of Fig. 1).

To quantify the shape of the density PDFs, we fit a log-normal and a Castaing-Hopkins model (Castaing 1996; Hopkins 2013; Federrath & Banerjee 2015; Seta et al. 2023) to the PDFs, in the log-density contrast (Passot & Vázquez-Semadeni 1998; Kritsuk et al. 2007; Federrath et al. 2010),

$$q = \ln(\rho/\langle \rho \rangle). \quad (16)$$

The log-normal (\mathcal{LN}) PDF is defined as

$$\mathcal{LN}(q) = \left(2\pi\sigma_{\mathcal{LN}}^2\right)^{-1/2} \exp\left[-\frac{1}{2}\left(\frac{q-\mu}{\sigma_{\mathcal{LN}}}\right)^2\right], \quad (17)$$

where $\mu = -\sigma_{\mathcal{LN}}^2/2$ is the mean and $\sigma_{\mathcal{LN}}^2$ is the variance. The Castaing-Hopkins (\mathcal{CH}) PDF is defined as

$$\mathcal{CH}(q) = I_1\left(2(\lambda\omega(q))^{-1/2}\right) \exp[-(\lambda + \omega(q))] \left(\frac{\lambda}{\theta_{\mathcal{CH}}^2\omega(q)}\right)^{-1},$$

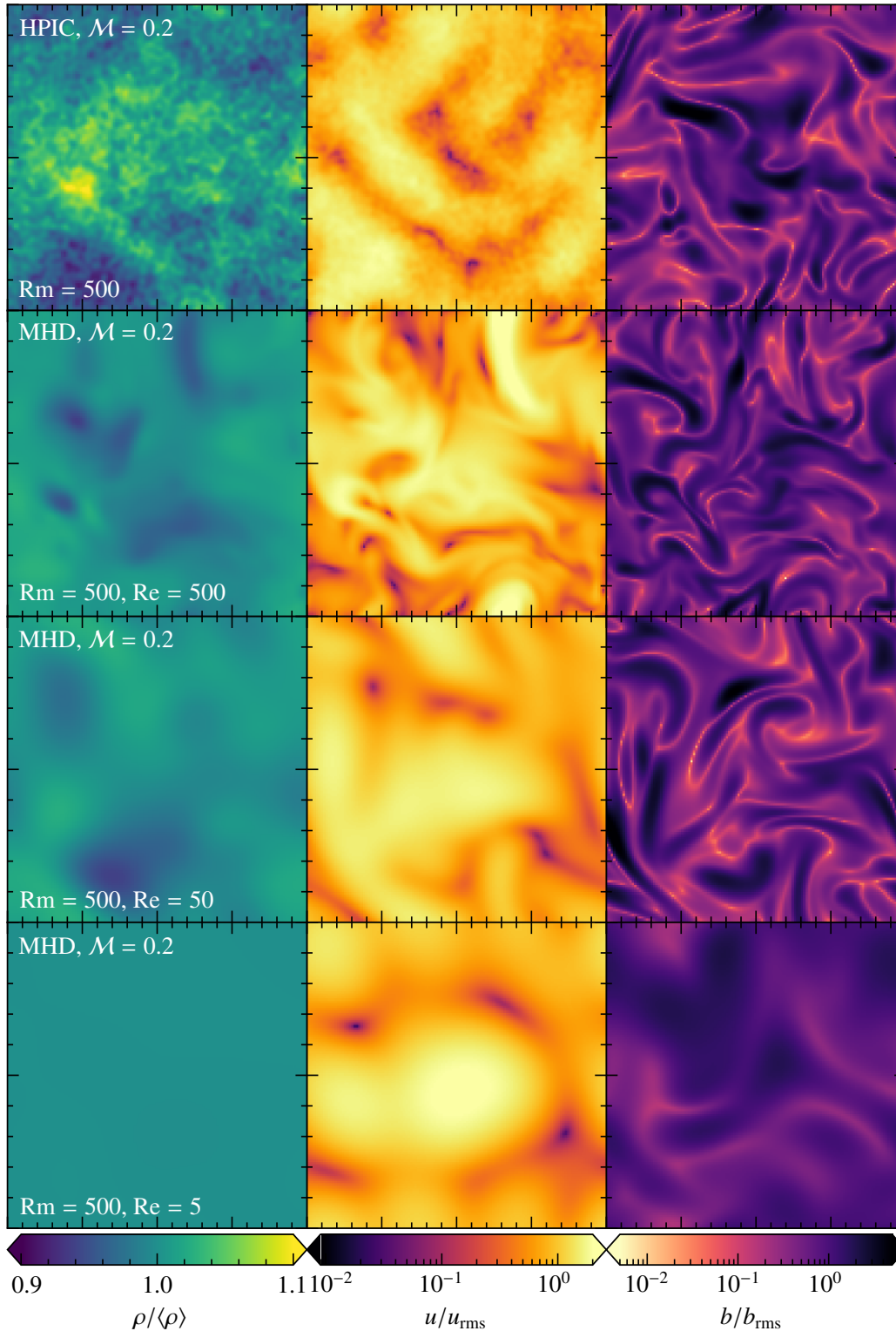


Figure 1. Slice through the mass density, normalised to the mean mass density, $\rho/\langle\rho\rangle$ (first column), the magnitude of velocity, normalised to the root mean square velocity, u/u_{rms} (second column), and the magnitude of the magnetic field, normalised to the root mean square magnetic field, b/b_{rms} (third column), for the subsonic ($\mathcal{M} = 0.2$) dynamo simulations in the middle of the kinematic regime ($t = 10 t_0$). The first row shows HPIC, while the 2nd to 4th rows show the MHD runs with $Re = 500, 50$, and 5 , respectively. We see that the density fluctuations (first column) are small ($\lesssim 10\%$), as expected for subsonic turbulence. The velocity structures (2nd column) for HPIC are visually similar to the MHD simulation with $Re = 50 - 500$. The magnetic field structure (3rd column) of HPIC resembles that of the MHD runs with $Re = 50$ and $Re = 500$. In the MHD runs, the fluctuations in ρ , u , and B decrease with decreasing Re , as expected due to the smoothing effect of enhanced viscosity. Apart from the expected small-scale particle noise in the HPIC run, the overall closest visual resemblance is between HPIC and the MHD runs with $Re \sim 50 - 500$.

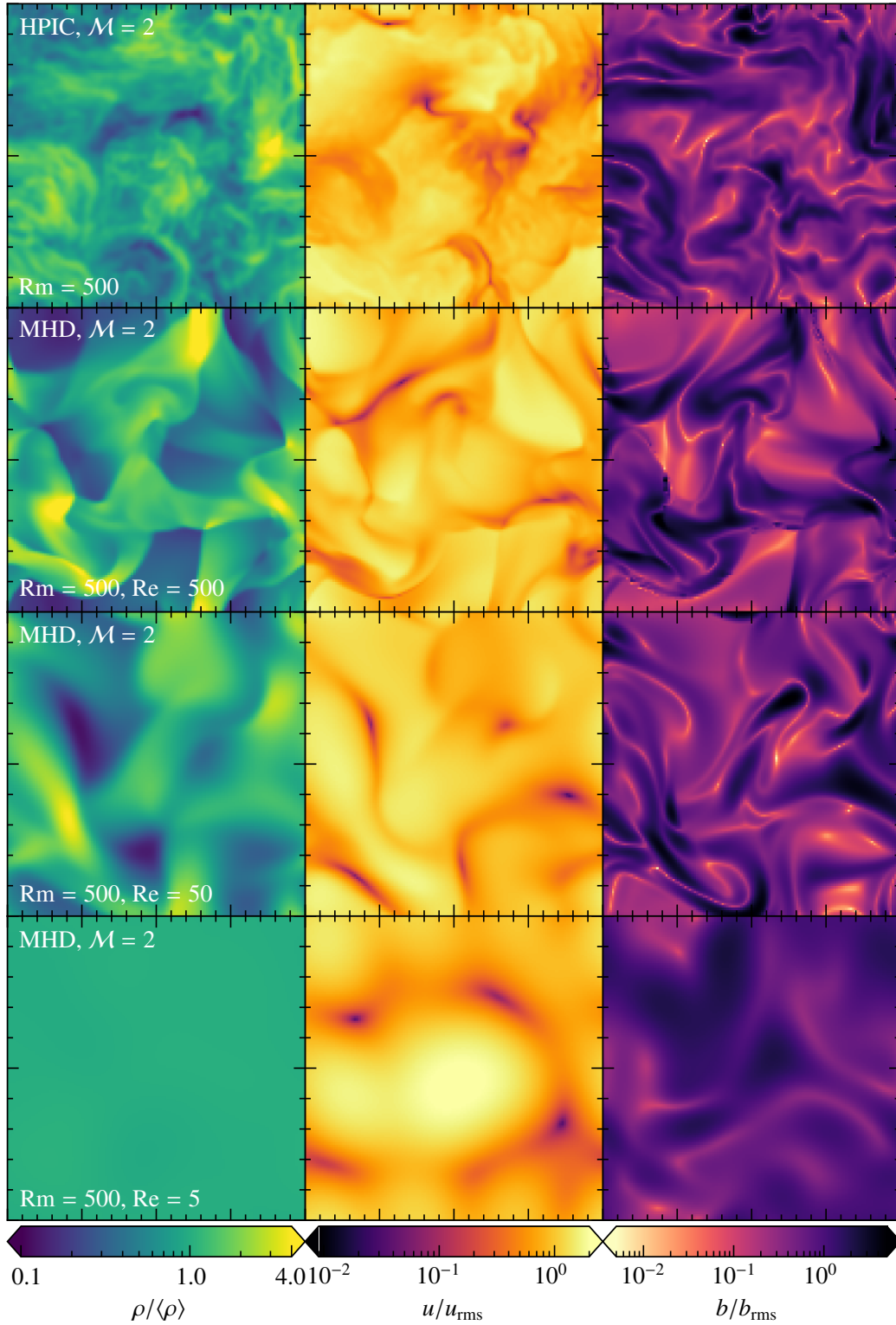


Figure 2. Same as Fig. 1, but for the supersonic regime ($\mathcal{M} = 2$). As expected, we see shock structures and large density contrasts emerging in this regime. Similar to the subsonic runs, also here the turbulent intermediate- and small-scale fluctuations decrease as Re decreases. The large-scale velocity structures show a significant correlation with the density structures in both HPIC and MHD, while the magnetic field has some large-scale correlation but also significant small-scale structure. The HPIC run is visually closest to the MHD $\text{Re} \sim 50 - 500$ runs in this supersonic regime.

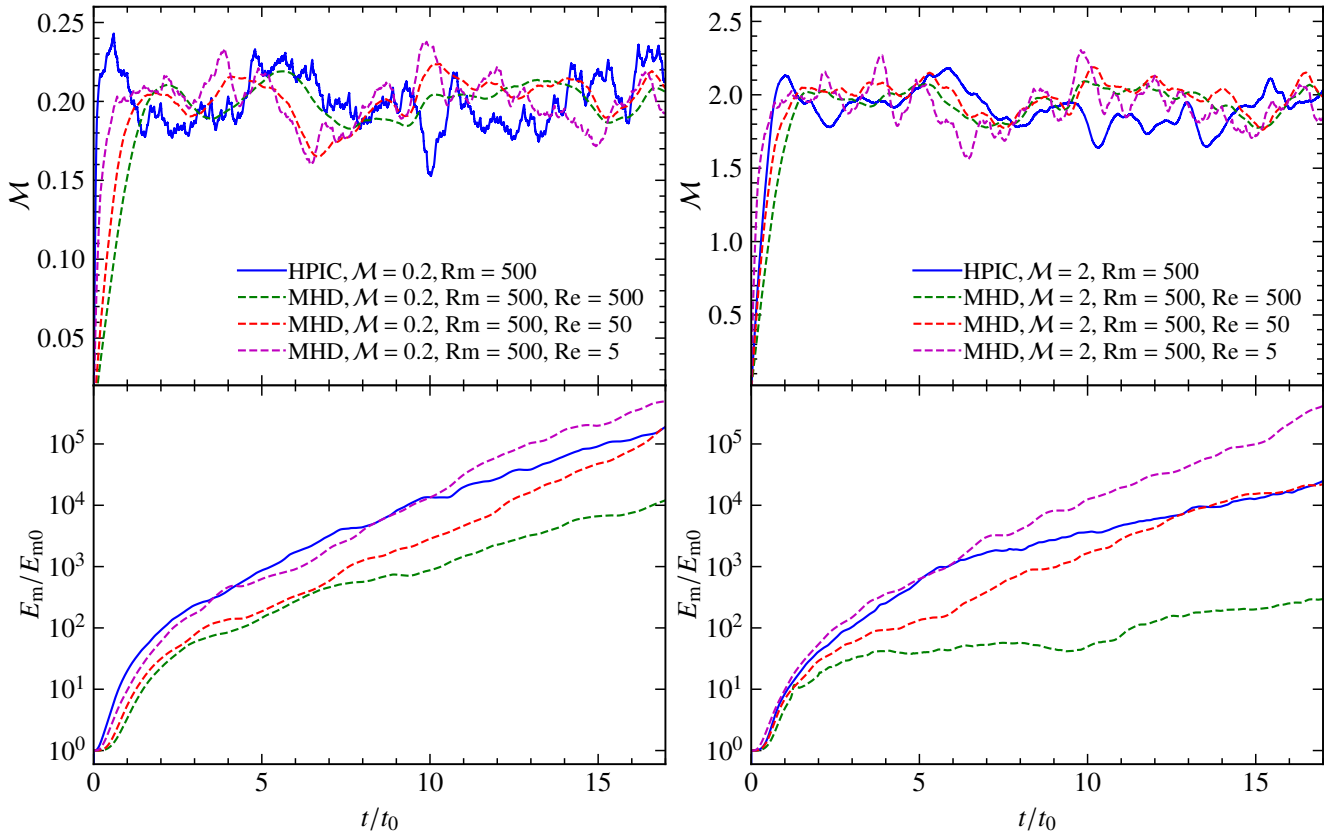


Figure 3. The Mach number, \mathcal{M} , and magnetic energy, normalised to the initial magnetic energy, E_m/E_{m0} , as a function of time, normalised to the eddy turn-over time, t_0 , for the HPIC (solid lines) and MHD turbulent dynamo runs (dashed lines). The left and right panels show the $\mathcal{M} = 0.2$ and 2 simulations, respectively. The measured Mach numbers and dynamo growth rates are reported in Tab. 1. The growth rate of the MHD runs increases as the Pm of the plasma increases (Re decreases), for both the $\mathcal{M} = 0.2$ and $\mathcal{M} = 2$ runs. The growth rate of the HPIC simulation is similar to that of the $\text{Re} = 5 - 500$ MHD runs ($\text{Pm} = 1 - 100$) in the subsonic regime, while in the supersonic regime, the HPIC run’s growth rate is similar to that of the $\text{Re} = 50 - 500$ MHD runs ($\text{Pm} = 1 - 10$).

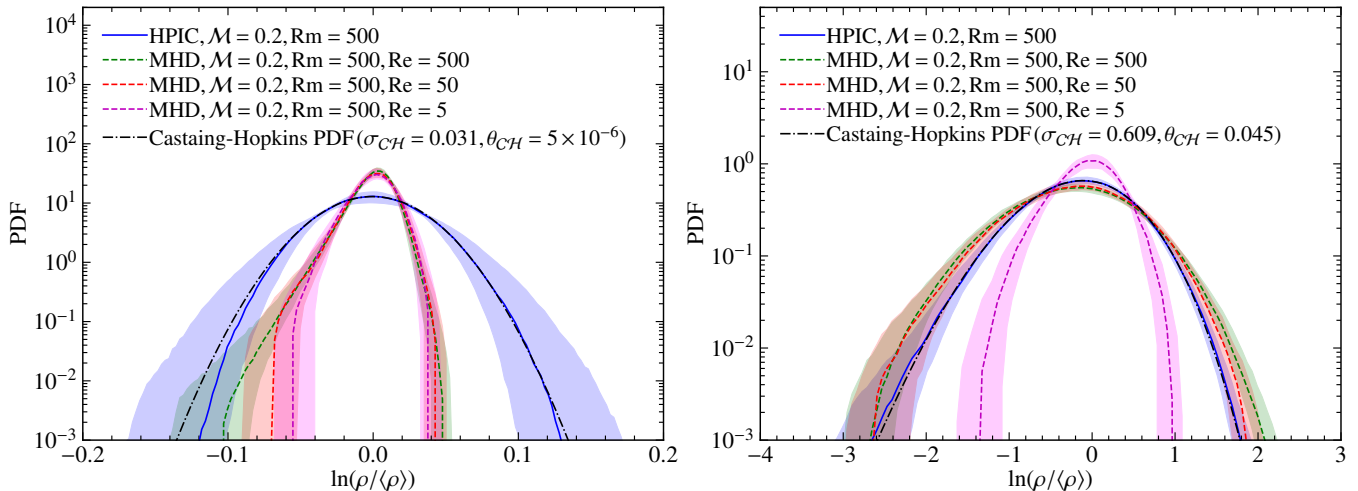


Figure 4. Probability density functions (PDFs) of the log-density contrast (Eq. 16), for HPIC (solid lines) and MHD (dashed lines) with $\mathcal{M} = 0.2$ (left panel) and 2 (right panel), respectively. The PDFs are time-averaged in the kinematic phase of the dynamo ($t/t_0 = 3 - 17$), with the lines and bands representing the median and the 16th to 84th percentile range, respectively. The magnitude of density fluctuations in the subsonic regime is much smaller than in the supersonic regime. For the MHD runs, we see that as Re decreases, the density fluctuations decrease due to viscosity suppressing fluctuations in the flow. We fit the density PDFs using the log-normal (Eq. 17) and the Castaing-Hopkins (Eq. 18) distribution and report the fit parameters in Tab. 2. The dash-dotted lines show the Castaing-Hopkins model fit for the HPIC simulations, as a representative example, providing a good fit for the supersonic case.

(18)

where $\lambda = \sigma_{C\mathcal{H}}^2 / (2\theta_{C\mathcal{H}}^2)$ and $\omega(q) = \lambda / (1 + \theta_{C\mathcal{H}}) - q / \theta_{C\mathcal{H}}$. Here I_1 is the modified Bessel function of the first kind, $\sigma_{C\mathcal{H}}^2$ is the variance, and $\theta_{C\mathcal{H}}$ is the intermittency parameter. The larger $\theta_{C\mathcal{H}}$, the stronger the intermittency. For $\theta_{C\mathcal{H}} \rightarrow 0$, the Castaing-Hopkins model reduces to the log-normal distribution.

All fit parameters are listed in Tab. 2. We find that the intermittency parameter, $\theta_{C\mathcal{H}} \rightarrow 0$, for the $\mathcal{M} = 0.2$ runs, and hence $\sigma_{C\mathcal{H}} \sim \sigma_{\mathcal{L}N}$, confirming that the log-normal is a good model in the subsonic regime. The intermittency parameter is much larger in the supersonic regime, as found in previous MHD simulations (Hopkins 2013; Federrath & Banerjee 2015). However, at $\mathcal{M} = 2$, $\theta_{C\mathcal{H}}$ is still relatively small, indicating that the log-normal is a reasonable model for density fluctuations in the mildly supersonic regime.

3.3.2 Velocity PDF

Fig. 5 shows the same as Fig. 4, but for the x -component of the velocity, u_x , normalised to the root mean square velocity, u_{rms} . We fit the velocity PDFs with a Gaussian (normal; \mathcal{N}) distribution by using $q = u_x / u_{\text{rms}}$ in Eq. 17, with $\mu_{\mathcal{N}}$ and $\sigma_{\mathcal{N}}$ as the mean and standard deviation, respectively. The fit parameters are listed in Tab. 2. The velocity PDFs of all simulations are in good agreement with a Gaussian distribution with $\mu_{\mathcal{N}} \sim 0$ and $\sigma_{\mathcal{N}} \sim 1/\sqrt{3}$, as expected for isotropic turbulence (e.g., see appendix in Federrath 2013). While we only show the x -component here, all 3 velocity components have very similar PDFs. This is indeed reflected in the fact that $\sigma_{\mathcal{N}} \sim 1/\sqrt{3}$ of a single component, i.e., when all 3 components are combined, we recover the target Mach number in each respective simulation. Finally, varying Re in the MHD runs does not significantly impact the shape of the velocity PDFs. However, increasing the viscosity would reduce u_{rms} for the same turbulence driving amplitude. Therefore, we adjust the driving amplitude (see Sec. 2.4) to ensure that the same target Mach numbers are reached for all choices of viscosity. The driving amplitude is fixed and does not vary dynamically throughout the simulation.

3.3.3 Magnetic field PDF

Finally, we study the magnetic field PDFs of the HPIC and MHD simulations. The PDFs of the x -component of the magnetic field, b_x , normalised to the root mean square magnetic field value, b_{rms} are shown in Fig. 6. We see that the magnetic field PDFs for all the simulations are non-Gaussian, with strong peaks around $b = 0$, reflecting the fact that mean fields are not present, and with very strong tails towards extreme b values. We model these PDFs using a Cauchy-normal distribution (Seta et al. 2021),

$$CN(q) = A \left[1 + \left(\frac{x - \mu_{CN}}{\gamma_{CN}} \right)^2 \right]^{-1} \exp \left[-\frac{1}{2} \left(\frac{x - \mu_{CN}}{\sigma_{CN}} \right)^2 \right], \quad (19)$$

where $q = b_x / b_{\text{rms}}$ and μ_{CN} , σ_{CN} , and γ_{CN} are the mean, the standard deviation of the normal part, and the scale of the Cauchy part, respectively. The coefficient

$$A = \frac{1}{2\pi^2 \gamma_{CN}} \exp \left[-\left(\frac{\gamma_{CN}}{2\sigma_{CN}} \right)^2 \right] \left[1 - \text{erf} \left(\frac{\gamma_{CN}}{\sqrt{2}\sigma_{CN}} \right) \right]^{-1}, \quad (20)$$

where erf is the error function, ensuring that the PDF is normalised, i.e., $\int CN(q) dq = 1$. Using this distribution function, we fit the magnetic field PDFs for all runs and list the fit parameters in Tab. 2.

The fits provide good approximations of the simulation data around the peak of the PDFs, with the tails being somewhat overestimated.

3.4 Spectra

In order to understand the characteristics of the plasma on different scales, we study the power spectra of magnetic energy, electric current, and turbulent kinetic energy.

3.4.1 Magnetic energy spectra

The magnetic energy power spectra of our simulations are shown in Fig. 7, with $\mathcal{M} = 0.2$ on the left and $\mathcal{M} = 2$ on the right. All the spectra shown henceforth are normalised such that the total power is unity and are also time-averaged in the kinematic regime of the dynamo. The lines represent the 50th percentile (median) of the data, and the shaded regions bracket the 16th to 84th percentile range. The $k^{3/2}$ scaling (dotted line), characteristic of the MHD turbulent dynamo in incompressible flows during the kinematic regime (Kazantsev 1968; Seta et al. 2020), also appears in the kinematic phase of compressive simulations (Seta & Federrath 2020, 2021a). This scaling shows reasonable agreement with all the simulations, both in the subsonic and supersonic regimes. However, the limited dynamic range at large scales (low k) prevents a detailed quantification of the scaling behaviour at those scales. Federrath et al. (2014) also find the $k^{3/2}$ scaling at much higher Mach numbers, $\mathcal{M} = 11$, in MHD simulations with a large magnetic Prandtl number, $\text{Pm} = 10$. For the MHD runs, the magnetic energy shifts to larger scales as Re decreases. The magnetic spectra for HPIC in both the subsonic and supersonic regimes are most similar to those of the respective MHD runs with $\text{Re} \sim 50 - 500$, although there are some significant differences across all scales.

3.4.2 Electric current spectra

Fig. 8 shows the spectra of the total current, $\mathbf{J} = (\nabla \times \mathbf{B}) / \mu_0$. Following the definition in Kriel et al. (2023), the peak wavenumber of the current spectra are used to represent the dissipation scale of the magnetic energy, i.e., the resistive wavenumber k_η . As in Kriel et al. (2023), the spectra are smoothed using a third-order cubic spline interpolation operator before obtaining k_η . The reported value and error are the mean and standard deviation of the peak wavenumber, as listed in Tab. 1. The k_η for the MHD runs decreases with Re , similar to the magnetic energy, which shifts to larger length scales as Re decreases. The magnetic dissipation scale for the $\mathcal{M} = 0.2$ HPIC run is comparable to that of the MHD simulation with $\text{Re} = 50 - 500$. For the $\mathcal{M} = 2$ HPIC run, it is more similar to the MHD run with $\text{Re} \sim 500$.

3.4.3 Turbulent kinetic energy spectra

The power spectra of the turbulent kinetic energy are shown in Fig. 9. The $k^{-5/3}$ Kolmogorov scaling, characteristic of subsonic turbulence and the k^{-2} Burgers scaling relation, characteristic of supersonic turbulence, are shown as guidelines for the $\text{Re} = 500$ MHD runs. The maximum turbulent energy is injected at $k_{\text{turb}} = 2$, as confirmed by the spectra. As the Re of the MHD simulations is decreased in both the $\mathcal{M} = 0.2$ and $\mathcal{M} = 2$ runs, the kinetic energy spectra get steeper, and the scaling range becomes shorter – it is practically absent in the $\text{Re} = 50$ and 5 runs, as expected, due to the low Reynolds numbers of these flows not allowing turbulent cascade to develop. The dissipation

Table 2. Fit parameters for the density ($\ln(\rho/\langle\rho\rangle)$) PDFs, and the x -components of the velocity (u_x/u_{rms}) and magnetic field (b_x/b_{rms}) PDFs.

Model	$\ln(\rho/\langle\rho\rangle)$			u_x/u_{rms}		b_x/b_{rms}		
	σ_{LN}	σ_{CH}	θ_{CH}	μ_N	σ_N	μ_{CN}	σ_{CN}	γ_{CN}
HPICM0.2Rm500	$0.031^{+0.001}_{-0.001}$	$0.031^{+0.001}_{-0.001}$	$5 \times 10^{-6+6 \times 10^{-4}}_{-4 \times 10^{-6}}$	$-0.002^{+0.013}_{-0.012}$	$0.573^{+0.012}_{-0.012}$	$0.000^{+0.007}_{-0.001}$	$2.670^{+1.817}_{-0.170}$	$0.224^{+0.076}_{-0.022}$
MHDM0.2Rm500Re500	$0.012^{+0.001}_{-0.001}$	$0.012^{+0.001}_{-0.001}$	$0.002^{+0.001}_{-0.001}$	$0.005^{+0.008}_{-0.009}$	$0.591^{+0.007}_{-0.007}$	$0.001^{+0.004}_{-0.001}$	$1.382^{+0.261}_{-0.153}$	$0.351^{+0.014}_{-0.018}$
MHDM0.2Rm500Re50	$0.013^{+0.001}_{-0.001}$	$0.013^{+0.001}_{-0.001}$	$0.002^{+0.001}_{-0.001}$	$-0.017^{+0.017}_{-0.019}$	$0.596^{+0.016}_{-0.015}$	$0.003^{+0.009}_{-0.003}$	$2.142^{+1.501}_{-0.499}$	$0.272^{+0.021}_{-0.021}$
MHDM0.2Rm500Re5	$0.014^{+0.001}_{-0.001}$	$0.014^{+0.001}_{-0.001}$	$0.002^{+0.001}_{-0.001}$	$0.000^{+0.016}_{-0.015}$	$0.580^{+0.015}_{-0.013}$	$0.001^{+0.005}_{-0.001}$	$2.548^{+1.676}_{-0.732}$	$0.237^{+0.020}_{-0.016}$
HPICM2Rm500	$0.595^{+0.009}_{-0.009}$	$0.609^{+0.011}_{-0.011}$	$0.045^{+0.010}_{-0.010}$	$0.000^{+0.013}_{-0.015}$	$0.580^{+0.012}_{-0.013}$	$0.000^{+0.005}_{-0.001}$	$2.085^{+1.501}_{-0.085}$	$0.242^{+0.058}_{-0.027}$
MHDM2Rm500Re500	$0.709^{+0.011}_{-0.010}$	$0.725^{+0.012}_{-0.012}$	$0.045^{+0.013}_{-0.012}$	$-0.027^{+0.012}_{-0.011}$	$0.588^{+0.011}_{-0.012}$	$0.001^{+0.007}_{-0.008}$	$2.543^{+1.239}_{-0.615}$	$0.242^{+0.015}_{-0.016}$
MHDM2Rm500Re50	$0.683^{+0.013}_{-0.013}$	$0.703^{+0.014}_{-0.016}$	$0.056^{+0.018}_{-0.015}$	$-0.016^{+0.015}_{-0.014}$	$0.590^{+0.014}_{-0.015}$	$0.000^{+0.008}_{-0.001}$	$2.529^{+2.462}_{-0.529}$	$0.237^{+0.063}_{-0.024}$
MHDM2Rm500Re5	$0.367^{+0.018}_{-0.016}$	$0.376^{+0.007}_{-0.006}$	$0.043^{+0.007}_{-0.006}$	$0.017^{+0.016}_{-0.015}$	$0.576^{+0.017}_{-0.015}$	$0.005^{+0.007}_{-0.005}$	$2.105^{+0.907}_{-0.217}$	$0.246^{+0.054}_{-0.019}$

Notes: The first three columns depict the lognormal (Eq. 17) and Castaing-Hopkins (Eq. 18) fit parameters for the density PDFs. The velocity PDFs are fit using a normal distribution and the fit parameters are shown in the fourth and fifth columns. The last three columns show the Cauchy-normal (Eq. 19) fit parameters for the magnetic field PDFs.

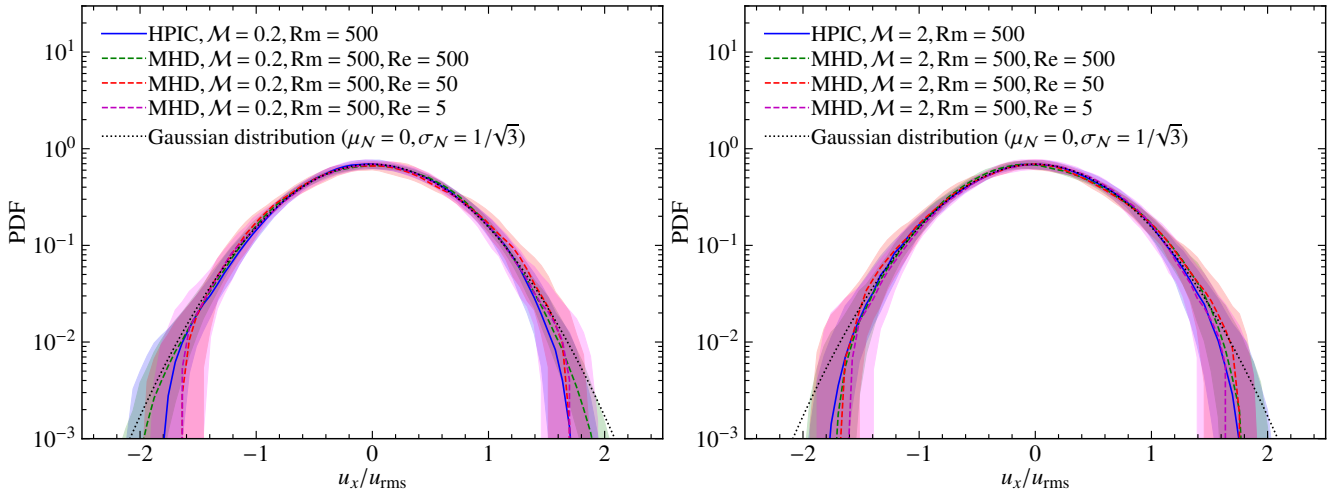


Figure 5. Same as Fig. 4, but for the x -component of the velocity, u_x , normalised to the root mean square velocity, u_{rms} . The dotted line shows a Gaussian function with mean, $\mu_N = 0$, and standard deviation, $\sigma_N = 1/\sqrt{3}$, for comparison. The velocity PDFs of all the simulations show good agreement with this Gaussian function.

scale of the turbulence shifts to larger length scales (smaller k) as the viscosity of the plasma increases. In the subsonic regime, the P_{kin} spectrum of HPIC resembles that of the $\text{Re} \sim 50 - 500$ MHD run. The spectrum of the supersonic HPIC run closely resembles the respective MHD run with $\text{Re} = 500$. This indicates that the $\mathcal{M} = 2$ HPIC run has a smaller viscosity in comparison to that of $\mathcal{M} = 0.2$ run. These findings are consistent with our earlier visual comparison of the velocity features in Figs. 1 and 2.

4 EFFECTIVE VISCOSITY AND KINETIC REYNOLDS NUMBER OF WEAKLY-COLLISIONAL PLASMAS

Here we first discuss the MHD scaling relations for the viscous and magnetic dissipation scales in Sec. 4.1, and then apply these to the

HPIC simulations in Sec. 4.2 to infer Re , k_ν , and Pm for weakly-collisional plasma.

4.1 MHD scaling relations for viscous and resistive scales

The viscous dissipation scale, $k_\nu = A k_{\text{turb}} \text{Re}^\alpha$, is related to the kinetic Reynolds number, where k_{turb} is the turbulence driving scale and A is a dimensionless scaling coefficient. Furthermore, the ratio of the magnetic and viscous dissipation scale, $k_\eta/k_\nu = B \text{Pm}^\beta$, can be expressed as a function of the magnetic Prandtl number (Kriel et al. 2022, 2023), B being another dimensionless scaling coefficient. MHD studies have investigated these scaling relations in the turbulent ($\text{Re} > 100$) and viscous ($\text{Re} < 100$) regimes separately (Kriel et al. 2023). The value of the coefficients, A and B , and the scaling exponents, α and β , in different Re regimes, are discussed in detail in Sec. 3.5 of Kriel et al. (2023). In this work, we provide a combined

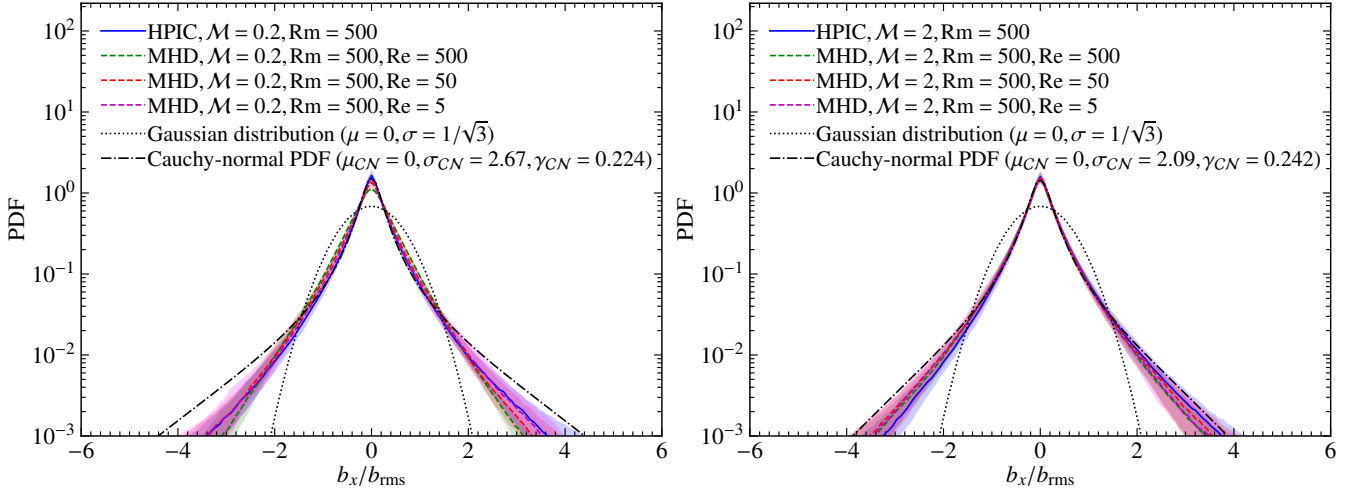


Figure 6. Same as Fig. 4, but for the x -component of the magnetic field, b_x , normalised to the root mean square magnetic field, b_{rms} . The dash-dotted lines show the Cauchy-normal fit (Eq. 19) for the HPIC simulations. The dotted line shows a Gaussian (Eq. 17) with $\mu = 0$ and $\sigma = 1/\sqrt{3}$ for comparison. The magnetic fields are clearly non-Gaussian (intermittent) in both the subsonic and supersonic regimes and show reasonable agreement with the Cauchy-normal function.

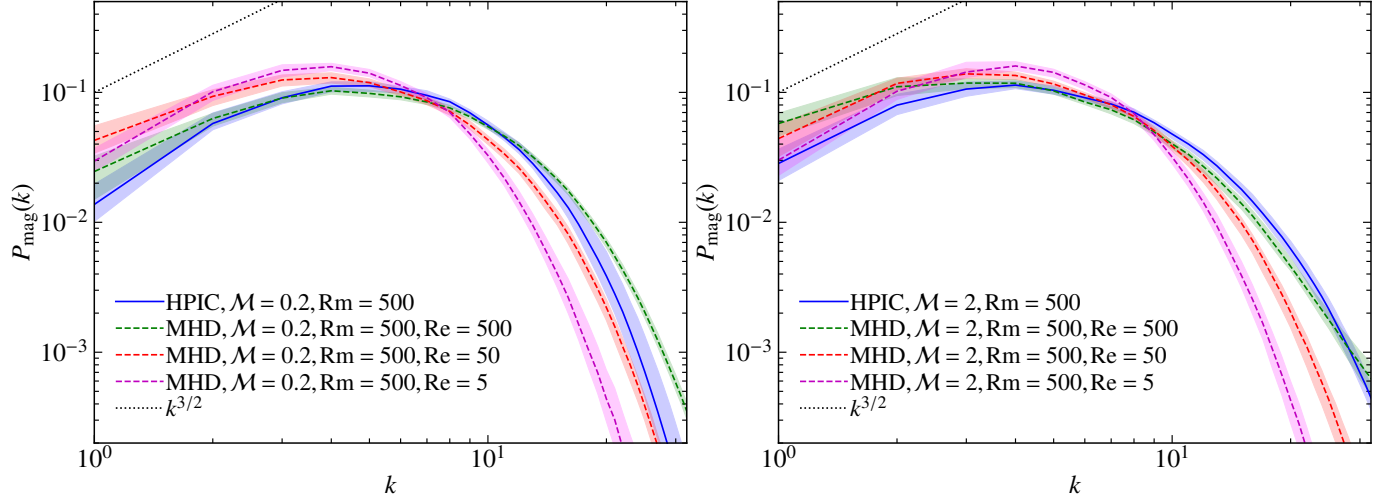


Figure 7. Magnetic energy power spectra for the HPIC (solid lines) and MHD (dashed lines) simulations with $\mathcal{M} = 0.2$ (left panel) and $\mathcal{M} = 2$ (right panel). The spectra presented here are time-averaged in the kinematic phase of the dynamo ($t = 3 - 17t_0$), and normalised to the total energy. The lines are the median (50th percentile) and the shaded regions range from the 16th to the 84th percentile, showing the time variation. The dotted line shows a $k^{3/2}$ scaling (Kazantsev 1968) for comparison. From the MHD runs, we see that as Re decreases, the magnetic energy moves to somewhat larger scales (lower k). Here HPIC is most similar to the MHD runs with $\text{Re} \sim 50 - 500$.

model across all Re values and refit the subsonic ($\mathcal{M} = 0.3$) and transonic ($\mathcal{M} = 1$) simulations from Kriel et al. (2023) with the present MHD runs, using a smoothly broken power-law function (motivated by the trends in the numerical results),

$$\mathcal{BP}(q) = C \left(\frac{q}{q_b} \right)^\alpha \left\{ \frac{1}{2} \left[1 + \left(\frac{q}{q_b} \right)^{1/\Delta} \right] \right\}^{(\beta - \alpha)\Delta}, \quad (21)$$

where $C = \mathcal{BP}(q_b)$ is the value of the model at the transition or break point q_b , α is the scaling exponent when $q \ll q_b$, β is the scaling exponent when $q \gg q_b$, and Δ controls how smoothly the transition of the scaling exponent from α to β occurs. We perform the fits for $k_\nu/k_{\text{turb}} = \mathcal{BP}(\text{Re})$ and $k_\eta/k_\nu = \mathcal{BP}(\text{Pm})$ using the Markov chain Monte Carlo method.

The parameters are determined by fitting the data from MHD simulations with varying Mach numbers: $\mathcal{M} = 0.2$ and 2, discussed

Table 3. Fit values for parameters in Eq. 21 shown in Fig. 10.

	C	q_b	α	β	Δ
$\mathcal{BP}(\text{Re})$	4.5 ± 1.0	105 ± 18	0.39 ± 0.02	$3/4$ (fixed)	1.8 ± 0.2
$\mathcal{BP}(\text{Pm})$	1.8 ± 0.3	18 ± 4	$1/2$ (fixed)	0.36 ± 0.02	0.25 ± 0.03

in this work, and $\mathcal{M} = 0.3$ and 1 from Kriel et al. (2023). The results are shown in Fig. 10 and the fit parameters are reported in Tab. 3. We find that the scaling relations describe the MHD data reasonably well for the subsonic and transonic simulations up to $\mathcal{M} = 2$. Only for $\mathcal{M} \gtrsim 5$ (not shown here), the relations change as one enters deeper into the supersonic regime, investigated in detail in Sec. 3.5 of Kriel et al. (2023).

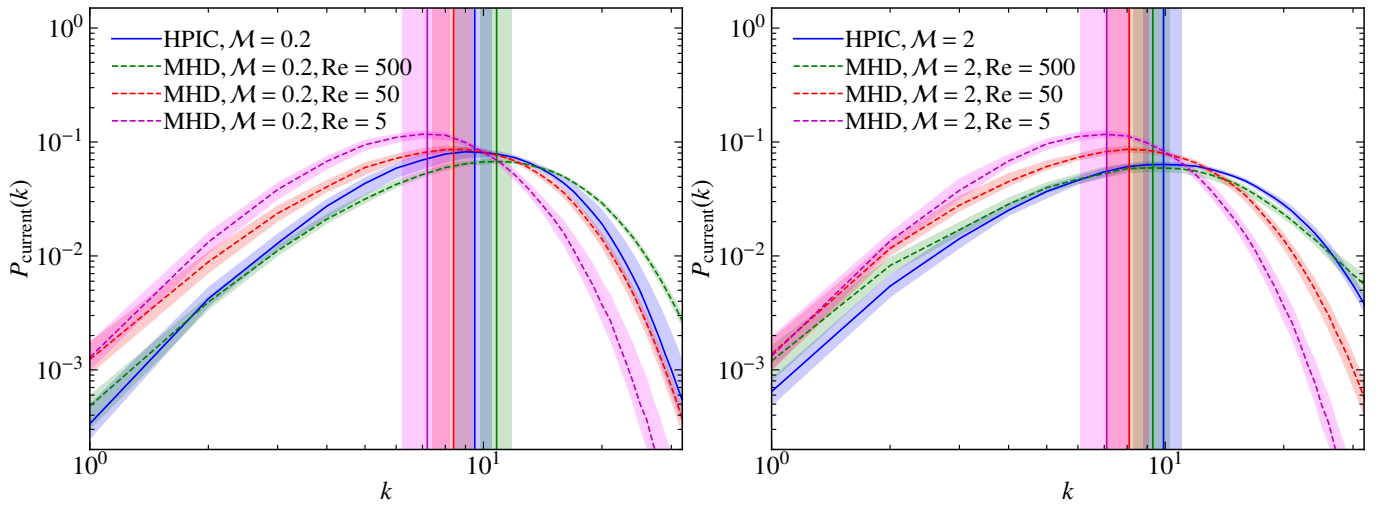


Figure 8. Same as Fig. 7 but for the total current. The peak of the current spectra corresponds to the scale of magnetic energy dissipation, k_η , indicated by the vertical solid lines, with the shaded region representing the error. The values of k_η are reported in Tab. 1. For the MHD runs, k_η decreases with Re. The k_η for the $\mathcal{M} = 0.2$ HPIC run is comparable to that of the MHD simulation with Re = 50–500, while for the $\mathcal{M} = 2$ HPIC run, it is similar to the MHD run with Re ~ 500 .

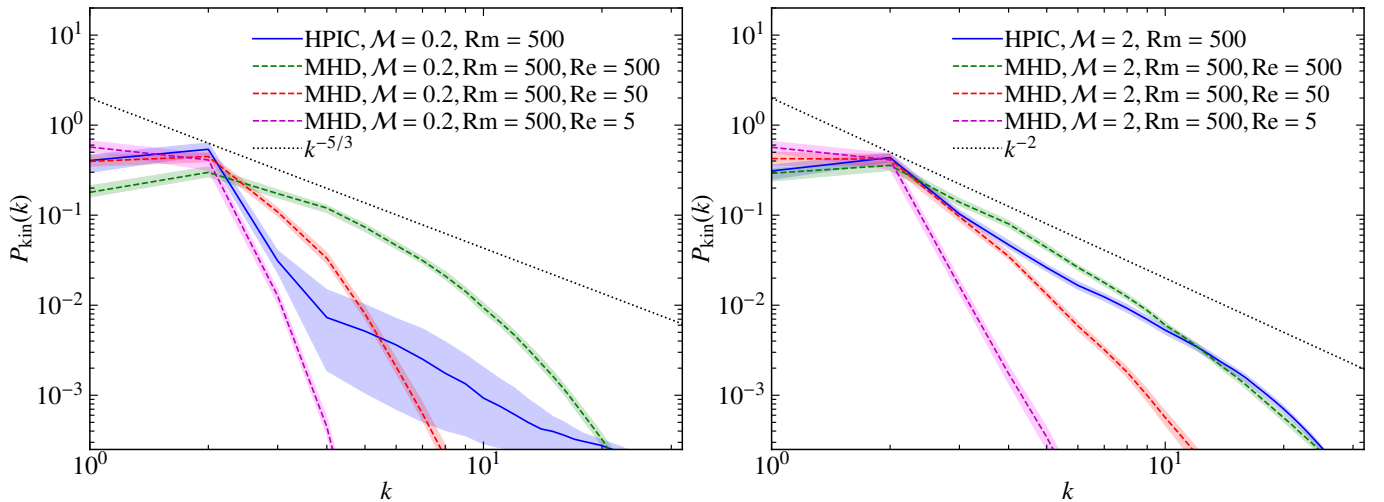


Figure 9. Same as Fig. 7 but for the turbulent kinetic energy. For comparison, we show the $k^{-5/3}$ Kolmogorov scaling, characteristic of subsonic turbulence (left panel) and the k^{-2} Burgers scaling (dotted lines), characteristic of supersonic turbulence (right panel). As Re decreases, both the scaling range and the dissipation wavenumber, k_ν , decrease. The two MHD simulations with Re = 500 agree reasonably with the Kolmogorov scaling in the subsonic regime, and the Burgers scaling in the supersonic regime, respectively. The spectrum of the subsonic HPIC run resembles that of the MHD run with Re $\sim 50 - 500$. In the supersonic regime, the HPIC run resembles the MHD run with Re = 500.

Using $k_\nu = k_{\text{turb}} \mathcal{B}\mathcal{P}(\text{Re})$ in the expression $k_\eta = k_\nu \mathcal{B}\mathcal{P}(\text{Pm})$, we can find Re from Rm (which is set via η for both the HPIC and MHD simulations) and k_η (which is determined from the peak of the current spectrum). Once Re is inferred, k_ν and Pm can be further estimated using Eq. 21 and Eq. 13, respectively. As a cross-check, this method is first applied on the MHD simulations themselves, with the results tabulated in Tab. 4, providing a reasonable recovery of Re and Pm in all cases, as expected, since the relations were calibrated (fitted) with those data (in addition to the data from Kriel et al. 2023). Furthermore, this analysis also helps us understand the level of uncertainties in these relations.

4.2 Application to HPIC simulations and the inferred Re, k_ν , and Pm

We now apply the MHD scaling relations from above to the HPIC runs. In contrast to the MHD case, for weakly-collisional plasmas, the Re (and thus k_ν) is a result of wave-particle interactions, and therefore not known or set a priori. Using the previously discussed MHD scaling relations, however, we can infer Re (and thus k_ν , and Pm) for the HPIC runs, assuming the MHD relations remain valid in weakly-collisional plasmas. The inferred value $\text{Re}_{\text{inferred}}$ is then used in Eq. 21 and Eq. 13 to determine the viscous dissipation scale, $(k_\nu)_{\text{inferred}}$, and the magnetic Prandtl number, $\text{Pm}_{\text{inferred}}$. The values of these plasma parameters are summarised in Tab. 5 for all HPIC runs.

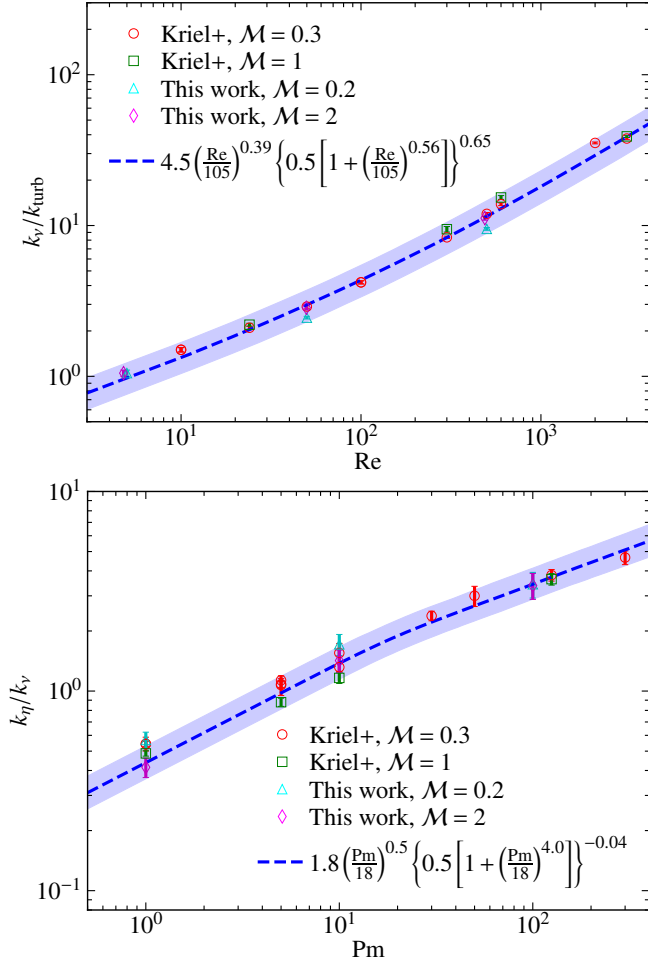


Figure 10. Viscous dissipation wavenumber, k_v , normalized by the turbulent driving scale, k_{turb} , as a function of the kinetic Reynolds number, Re (top panel), and ratio of magnetic to viscous dissipation wavenumber, k_η/k_v , as a function of the magnetic Prandtl number, Pm (bottom panel). We show MHD simulations with $\mathcal{M} = 0.3$ (circles) and 1 (squares) from Kriel et al. (2023), along with the $\mathcal{M} = 0.2$ (triangles) and 2 (diamonds) runs of this work. The dashed lines represent the median value of the fits using Eq. 21. The shaded region corresponds to the 16th (lower) and 84th (upper) percentile values. We find that all runs, i.e., subsonic and transonic runs up to $\mathcal{M} = 2$ as investigated here, are consistent with the same scaling relations. The fitted relations and associated parameter values are listed in Tab. 3.

For the standard $\mathcal{M} = 0.2$ HPIC run discussed in this work, the inferred kinetic Reynolds number, $\text{Re}_{\text{inferred}} = 480^{+170}_{-250}$. This corresponds to $(k_v)_{\text{inferred}} = 23^{+4.9}_{-8.5}$ and $\text{Pm}_{\text{inferred}} = 1.1^{+1.1}_{-0.38}$. In the standard $\mathcal{M} = 2$ HPIC run, the inferred values are $\text{Re}_{\text{inferred}} = 690^{+360}_{-360}$ and $(k_v)_{\text{inferred}} = 29^{+9.2}_{-11}$, which are somewhat larger than those in the subsonic regime. The corresponding $\text{Pm}_{\text{inferred}} = 0.72^{+0.71}_{-0.29}$ is somewhat lower compared to the subsonic case. While varying the number of particles per cell does not significantly affect these values, increasing the grid resolution raises the viscous dissipation scale and therefore the Re somewhat. This is because the magnetic dissipation scale increases marginally with grid resolution and with $N_{\text{grid}}^3 = 64^3$, $\text{Rm} = 500$ may not be resolved (Malvadi Shivakumar & Federrath 2023).

A caveat of this approach is that the scaling relations used here are derived from numerical simulations of the MHD turbulent dynamo,

Table 4. The inferred kinetic Reynolds number, $\text{Re}_{\text{inferred}}$, the viscous dissipation scale, $(k_v)_{\text{inferred}}$, and the magnetic Prandtl number, $\text{Pm}_{\text{inferred}}$, for the $\mathcal{M} = 0.2$ and $\mathcal{M} = 2$ runs with $N_{\text{grid}}^3 = 128^3$. The values are the median (50th percentile) of the data. The lower and upper error bars show the 16th – 50th and 84th – 50th percentile of the data, respectively.

Model	$\text{Re}_{\text{inferred}}$	$(k_v)_{\text{inferred}}$	$\text{Pm}_{\text{inferred}}$
MHDM0.2Rm500Re500	780^{+560}_{-340}	$31^{+13}_{-9.7}$	$0.64^{+0.53}_{-0.28}$
MHDM0.2Rm500Re50	74^{+220}_{-24}	$7.4^{+9.2}_{-1.4}$	$6.8^{+4.2}_{-5.0}$
MHDM0.2Rm500Re5	$10^{+45}_{-5.6}$	$2.7^{+3.6}_{-0.8}$	47^{+68}_{-38}
MHDM2Rm500Re500	490^{+120}_{-260}	$23^{+3.6}_{-8.8}$	$1.1^{+1.1}_{-0.27}$
MHDM2Rm500Re50	$41^{+190}_{-2.4}$	$5.4^{+8.8}_{-0.17}$	$11^{+2.2}_{-9.4}$
MHDM2Rm500Re5	$10^{+65}_{-5.5}$	$2.7^{+4.8}_{-0.8}$	48^{+59}_{-42}

Table 5. Same as Tab. 4, but for the HPIC simulations.

Model	$\text{Re}_{\text{inferred}}$	$(k_v)_{\text{inferred}}$	$\text{Pm}_{\text{inferred}}$
HPICM0.2Rm500	480^{+170}_{-250}	$23^{+4.9}_{-8.5}$	$1.1^{+1.1}_{-0.38}$
HPICM2Rm500	690^{+360}_{-360}	$29^{+9.2}_{-11}$	$0.72^{+0.71}_{-0.29}$
HPICM0.2Rm500Nppc50	470^{+300}_{-230}	$22^{+8.4}_{-7.6}$	$1.1^{+0.98}_{-0.47}$
HPICM0.2Rm500Nppc200	480^{+200}_{-250}	$23^{+5.7}_{-8.3}$	$1.1^{+1.0}_{-0.41}$
HPICM2Rm500Nppc50	670^{+410}_{-340}	28^{+11}_{-10}	$0.73^{+0.69}_{-0.31}$
HPICM2Rm500Nppc200	690^{+440}_{-340}	29^{+11}_{-10}	$0.72^{+0.62}_{-0.31}$
HPICM0.2Rm500Ngrid64	190^{+310}_{-73}	$13^{+10}_{-3.1}$	$2.5^{+1.8}_{-1.6}$
HPICM0.2Rm500Ngrid256	440^{+180}_{-240}	$21^{+5.2}_{-8.1}$	$1.2^{+1.3}_{-0.45}$
HPICM2Rm500Ngrid64	230^{+330}_{-100}	$14^{+11}_{-4.2}$	$2.0^{+1.6}_{-1.2}$
HPICM2Rm500Ngrid256	770^{+820}_{-320}	$31^{+19}_{-9.2}$	$0.63^{+0.49}_{-0.32}$

which may not be directly applicable to the weakly-collisional and collisionless regime. Additionally, this approach assumes that the plasma viscosity is isotropic in space and remains unchanged in the kinematic regime of the dynamo. These assumptions may not hold true for weakly-collisional plasma. Nevertheless, the approach seems to provide reasonable estimates of Re , which are at least in qualitative agreement with other flow characteristics such as the basic structure, dynamics, and statistics of the plasma (c.f., Figs 1 and 2 and following).

5 CONCLUSIONS

We study the properties of the weakly-collisional hybrid particle-in-cell (HPIC) turbulent dynamo in the subsonic ($\mathcal{M} = 0.2$) and supersonic ($\mathcal{M} = 2$) regimes in the kinematic phase using the HPIC code AHKASH and compare its properties to the collisional MHD turbulent dynamo. We use the same turbulence driving, magnetic Reynolds number, $\text{Rm} = 500$, and initial magnetic to kinetic en-

ergy ratio, $(E_{\text{mag}}/E_{\text{kin}})_0 = 10^{-10}$, for all the simulations (HPIC and MHD). For the HPIC simulations, a cooling method is used to maintain isothermal conditions and the initial ratio of the Larmor radius to the box size, $(r_{\text{Larmor}}/L)_0 = 100$. The MHD runs have varying kinetic Reynolds and magnetic Prandtl number, $\text{Re} = 500$ ($\text{Pm} = 1$), $\text{Re} = 50$ ($\text{Pm} = 10$) and $\text{Re} = 5$ ($\text{Pm} = 100$).

We compare the spatial structure, the growth rate of magnetic energy, the probability density functions (PDFs), and the power spectra of the HPIC and MHD simulations. We find that the density, velocity, and magnetic field structure of the HPIC runs is visually the closest to the MHD simulations with $\text{Re} \sim 50 - 500$, as discussed in Sec. 3.1. The growth rate of magnetic energy in HPIC is similar to that of MHD with $\text{Pm} = 1 - 100$ in the subsonic regime of turbulence, whereas in the supersonic regime, it resembles that of MHD with $\text{Pm} = 1 - 10$, as shown in Sec. 3.2.

We fit the density PDFs with a lognormal and a Castaing-Hopkins distribution in Sec. 3.3.1 and find that the lognormal distribution is a suitable model for all runs. For the velocity PDF, discussed in Sec. 3.3.2, a Gaussian distribution with mean ~ 0 and standard deviation $\sim 1/\sqrt{3}$ fits well, as expected. The magnetic field PDFs are fit with a Cauchy-normal distribution, showing that both MHD and HPIC turbulent dynamo exhibit highly intermittent magnetic fields (see Sec. 3.3.3).

The magnetic energy power spectra of HPIC are similar to those of MHD with $\text{Re} \sim 50 - 500$, as shown in Sec. 3.4.1. We find that the dissipation scale of the magnetic energy, k_{η} , of the HPIC runs, is 9.5 ± 1.0 and 9.9 ± 1.1 in the subsonic and supersonic regime, respectively. The magnetic dissipation scale for the subsonic HPIC run is comparable to that of the MHD simulation with $\text{Re} = 50-500$, while for the supersonic HPIC run, it is similar to the MHD run with $\text{Re} = 500$ (see Sec. 3.4.2). The turbulent kinetic energy power spectrum in the subsonic HPIC run is similar to the respective MHD runs with $\text{Re} \sim 50 - 500$, while in the supersonic case, it is similar to the MHD run with $\text{Re} \sim 500$, as discussed in Sec. 3.4.3. Applying scaling relations determined from studies of the MHD turbulent dynamo in Sec. 4.1, we find $\text{Re} = 480^{+170}_{-250}$ for subsonic HPIC, while supersonic HPIC has $\text{Re} = 690^{+360}_{-360}$, as discussed in Sec. 4.2. The corresponding viscous dissipation scale, $k_{\nu} = 23^{+4.9}_{-8.5}$ and $29^{+9.2}_{-11}$ in the subsonic and supersonic HPIC runs, respectively.

Overall, we find that the turbulent dynamo exhibits similar physical properties in weakly-collisional (HPIC) and collisional (MHD) plasmas. For subsonic turbulence, the present HPIC simulations share similarities with MHD at $\text{Re} \sim 50 - 500$, while in the supersonic regime, HPIC is similar to MHD at $\text{Re} \sim 500$. To the best of our knowledge, this is the first time that the weakly-collisional plasma dynamo has been studied in the supersonic regime of turbulence, which may be relevant for weakly-collisional shocks (e.g., potentially in supernovae or the supersonic regions of the solar wind), and the compressible regions of the galaxy intracluster medium (ICM).

ACKNOWLEDGEMENTS

R. A. C. acknowledges financial support from the Australian Government via the Australian Government Research Training Program Fee-Offset Scholarship. R. A. C. also acknowledges that this work was supported by an NCI HPC-AI Talent Program 2023 Scholarship (project gp08), with computational resources provided by NCI Australia, an NCRIS-enabled capability supported by the Australian Government. C. F. acknowledges funding provided by the Australian Research Council (Discovery Project grants DP230102280

and DP250101526), and the Australia-Germany Joint Research Cooperation Scheme (UA-DAAD). A. S. acknowledges support from the Australian Research Council's Discovery Early Career Researcher Award (DECRA, project DE250100003). We further acknowledge high-performance computing resources provided by the Leibniz Rechenzentrum and the Gauss Centre for Supercomputing (grants pr32lo, pr48pi, pn76ga and GCS Large-scale project 10391), the Australian National Computational Infrastructure (grant ek9) and the Pawsey Supercomputing Centre (project pawsey0810) in the framework of the National Computational Merit Allocation Scheme and the ANU Merit Allocation Scheme. The simulation software, FLASH, was in part developed by the Flash Centre for Computational Science at the University of Chicago and the Department of Physics and Astronomy at the University of Rochester.

DATA AVAILABILITY

The simulation data (5 TB) will be shared on reasonable request to the corresponding author.

REFERENCES

- Achikanath Chirakkara R., Federrath C., Trivedi P., Banerjee R., 2021, *Phys. Rev. Lett.*, **126**, 091103
- Achikanath Chirakkara R., Seta A., Federrath C., Kunz M. W., 2024a, *MNRAS*, **528**, 937
- Achikanath Chirakkara R., Federrath C., Seta A., 2024b, *MNRAS*, **534**, 3761
- Ackermann M., et al., 2018, *ApJS*, **237**, 32
- Beattie J. R., Federrath C., Kriel N., Mocz P., Seta A., 2023, *MNRAS*, **524**, 3201
- Bhat P., Subramanian K., 2013, *MNRAS*, **429**, 2469
- Bonafede A., Feretti L., Murgia M., Govoni F., Giovannini G., Dallacasa D., Dolag K., Taylor G. B., 2010, *A&A*, **513**, A30
- Bonafede A., Vazza F., Brüggén M., Murgia M., Govoni F., Feretti L., Giovannini G., Ogrean G., 2013, *MNRAS*, **433**, 3208
- Bott A. F. A., et al., 2021a, *Proceedings of the National Academy of Science*, **118**, e2015729118
- Bott A. F. A., et al., 2021b, *Phys. Rev. Lett.*, **127**, 175002
- Botteon A., et al., 2022, *Science Advances*, **8**, eabq7623
- Bouchut F., Klingenberg C., Waagan K., 2007, *Numerische Mathematik*, **108**, 7
- Bouchut F., Klingenberg C., Waagan K., 2010, *Numerische Mathematik*, **115**, 647
- Brandenburg A., Subramanian K., 2005, *Phys. Rep.*, **417**, 1
- Castaing B., 1996, *Journal de Physique II*, **6**, 105
- Chen L. E., et al., 2020, *ApJ*, **892**, 114
- Cho J., Vishniac E. T., Beresnyak A., Lazarian A., Ryu D., 2009, *ApJ*, **693**, 1449
- Dubey A., Reid L. B., Fisher R., 2008a, *Physica Scripta Volume T*, **132**, 014046
- Dubey A., et al., 2008b, in Pogorelov N. V., Audit E., Zank G. P., eds, *Astronomical Society of the Pacific Conference Series Vol. 385, Numerical Modeling of Space Plasma Flows*. p. 145
- Federrath C., 2013, *MNRAS*, **436**, 1245
- Federrath C., 2016, *Journal of Plasma Physics*, **82**, 535820601
- Federrath C., Banerjee S., 2015, *MNRAS*, **448**, 3297
- Federrath C., Klessen R. S., Schmidt W., 2008, *ApJ*, **688**, L79
- Federrath C., Roman-Duval J., Klessen R. S., Schmidt W., Mac Low M. M., 2010, *A&A*, **512**, A81
- Federrath C., Chabrier G., Schober J., Banerjee R., Klessen R. S., Schleicher D. R. G., 2011a, *Phys. Rev. Lett.*, **107**, 114504
- Federrath C., Sur S., Schleicher D. R. G., Banerjee R., Klessen R. S., 2011b, *ApJ*, **731**, 62
- Federrath C., Schober J., Bovino S., Schleicher D. R. G., 2014, *ApJ*, **797**, L19

Federrath C., Klessen R. S., Iapichino L., Beattie J. R., 2021, *Nature Astronomy*, 5, 365

Federrath C., Roman-Duval J., Klessen R. S., Schmidt W., Mac Low M. M., 2022, TG: Turbulence Generator, Astrophysics Source Code Library, record ascl:2204.001 (ascl:2204.001)

Ferrière K., 2020, *Plasma Physics and Controlled Fusion*, 62, 014014

Finke J. D., Reyes L. C., Georganopoulos M., Reynolds K., Ajello M., Fegan S. J., McCann K., 2015, *ApJ*, 814, 20

Fryxell B., et al., 2000, *ApJS*, 131, 273

Gatuzz E., Sanders J. S., Dennerl K., Pinto C., Fabian A. C., Tamura T., Walker S. A., ZuHone J., 2022a, *MNRAS*, 511, 4511

Gatuzz E., et al., 2022b, *MNRAS*, 513, 1932

Gatuzz E., et al., 2023, *MNRAS*, 522, 2325

Gent F. A., Mac Low M.-M., Korpi-Lagg M. J., Singh N. K., 2023, *ApJ*, 943, 176

Haugen N. E. L., Brandenburg A., Mee A. J., 2004, *MNRAS*, 353, 947

Hew J. K. J., Federrath C., 2023, *MNRAS*, 520, 6268

Hitomi Collaboration et al., 2016, *Nature*, 535, 117

Hoang D. N., et al., 2017, *MNRAS*, 471, 1107

Hopkins P. F., 2013, *MNRAS*, 430, 1880

Hu Y., Xu S., Stone J. M., Lazarian A., 2022, *ApJ*, 941, 133

Kazantsev A. P., 1968, *Soviet Journal of Experimental and Theoretical Physics*, 26, 1031

Konstandin L., Federrath C., Klessen R. S., Schmidt W., 2012, *Journal of Fluid Mechanics*, 692, 183

Kowal G., Lazarian A., Beresnyak A., 2007, *ApJ*, 658, 423

Kriel N., Beattie J. R., Seta A., Federrath C., 2022, *MNRAS*,

Kriel N., Beattie J. R., Federrath C., Krumholz M. R., Hew J. K. J., 2023, *arXiv e-prints*, p. [arXiv:2310.17036](https://arxiv.org/abs/2310.17036)

Kritsuk A. G., Norman M. L., Padoan P., Wagner R., 2007, *ApJ*, 665, 416

Kulsrud R. M., 2005, *Plasma physics for astrophysics*

Kunz M. W., Jones T. W., Zhuravleva I., 2022, *arXiv e-prints*, p. [arXiv:2205.02489](https://arxiv.org/abs/2205.02489)

Malvadi Shivakumar L., Federrath C., 2023, *arXiv e-prints*, p. [arXiv:2311.10350](https://arxiv.org/abs/2311.10350)

Moffatt H. K., 1978, *Magnetic field generation in electrically conducting fluids*

Neronov A., Vovk I., 2010, *Science*, 328, 73

Padoan P., Nordlund A., Jones B. J. T., 1997, *MNRAS*, 288, 145

Passot T., Vázquez-Semadeni E., 1998, *Phys. Rev. E*, 58, 4501

Rincon F., Califano F., Schekochihin A. A., Valentini F., 2016, *Proceedings of the National Academy of Science*, 113, 3950

Rosin M. S., Schekochihin A. A., Rincon F., Cowley S. C., 2011, *MNRAS*, 413, 7

Schekochihin A. A., Cowley S. C., 2006, *Physics of Plasmas*, 13, 056501

Schekochihin A. A., Cowley S. C., Taylor S. F., Maron J. L., McWilliams J. C., 2004, *ApJ*, 612, 276

Schober J., Schleicher D. R. G., Klessen R. S., 2013, *A&A*, 560, A87

Seta A., Federrath C., 2020, *MNRAS*, 499, 2076

Seta A., Federrath C., 2021a, *Physical Review Fluids*, 6, 103701

Seta A., Federrath C., 2021b, *MNRAS*, 502, 2220

Seta A., Federrath C., 2022, *MNRAS*, 514, 957

Seta A., Bushby P. J., Shukurov A., Wood T. S., 2020, *Physical Review Fluids*, 5, 043702

Seta A., Rodrigues L. F. S., Federrath C., Hales C. A., 2021, *ApJ*, 907, 2

Seta A., Federrath C., Livingston J. D., McClure-Griffiths N. M., 2023, *MNRAS*, 518, 919

Simionescu A., et al., 2019, *Space Sci. Rev.*, 215, 24

Sironi L., Comisso L., Golant R., 2023, *Phys. Rev. Lett.*, 131, 055201

St-Onge D. A., Kunz M. W., 2018, *ApJ*, 863, L25

St-Onge D. A., Kunz M. W., Squire J., Schekochihin A. A., 2020, *Journal of Plasma Physics*, 86, 905860503

Subramanian K., Shukurov A., Haugen N. E. L., 2006, *MNRAS*, 366, 1437

Sur S., 2019, *MNRAS*, 488, 3439

Sur S., Schleicher D. R. G., Banerjee R., Federrath C., Klessen R. S., 2010, *ApJ*, 721, L134

Tavecchio F., Ghisellini G., Foschini L., Bonnoli G., Ghirlanda G., Coppi P., 2010, *MNRAS*, 406, L70

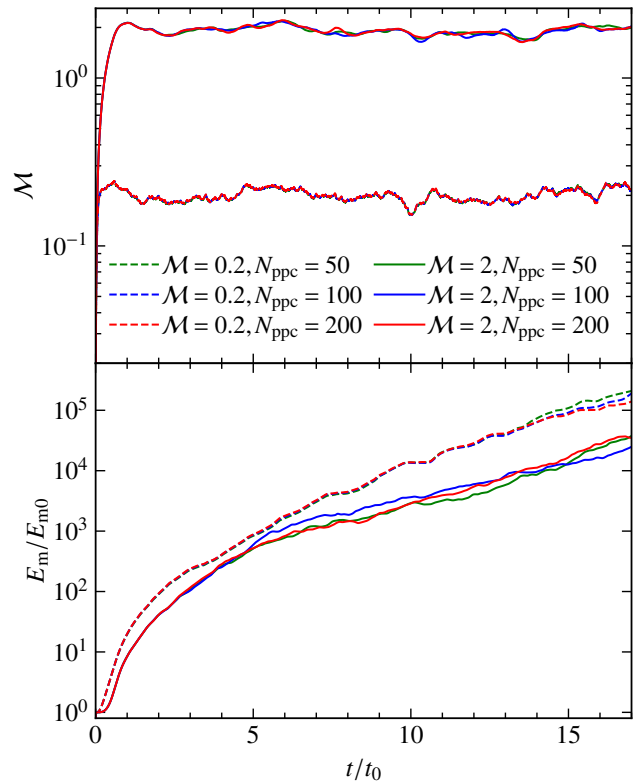


Figure A1. Same as Fig. 3, but for subsonic and supersonic weakly-collisional turbulent dynamo simulations with fixed grid resolution $N_{\text{grid}}^3 = 128^3$ and varying $N_{\text{ppc}} = 50, 100$ and 200 particles per cell. The Mach number and magnetic energy growth rate are tabulated in Tab. 1. The numerical simulations show convergence with $N_{\text{ppc}} = 100$.

Taylor A. M., Vovk I., Neronov A., 2011, *A&A*, 529, A144

Tzeferacos P., et al., 2017, *Physics of Plasmas*, 24, 041404

Tzeferacos P., et al., 2018, *Nature Communications*, 9, 591

Vázquez-Semadeni E., 1994, *ApJ*, 423, 681

Vazza F., Brunetti G., Brügggen M., Bonafede A., 2018, *MNRAS*, 474, 1672

Vovk I., Taylor A. M., Semikoz D., Neronov A., 2012, *ApJ*, 747, L14

Waagan K., Federrath C., Klingenberg C., 2011, *Journal of Computational Physics*, 230, 3331

Xu S., Lazarian A., 2016, *ApJ*, 833, 215

Zhou M., Zhdankin V., Kunz M. W., Loureiro N. F., Uzdensky D. A., 2024, *ApJ*, 960, 12

APPENDIX A: PARTICLE AND GRID RESOLUTION CONVERGENCE TESTS FOR HYBRID PIC SIMULATIONS

To show the convergence of our $\mathcal{M} = 0.2$ and $\mathcal{M} = 2$ simulations, we repeat our numerical experiments with varying grid resolutions and number of particles per cell. The time evolution of the HPIC runs with a fixed grid resolution ($N_{\text{grid}}^3 = 128^3$) and varying particle resolution of $N_{\text{ppc}} = 50, 100$, and 200 particles per cell is shown in Fig. A1. We do not find any significant difference in the time evolution of the dynamo as the number of particles per cell is changed.

The time evolution of the HPIC simulations with a fixed number of particles-per-cell ($N_{\text{ppc}} = 100$) and varying grid resolution of 64^3 , 128^3 , and 256^3 is shown in Fig. A2. We find that the Mach number and magnetic energy growth rate are converged with $N_{\text{grid}}^3 = 128^3$ (see Tab. 1).

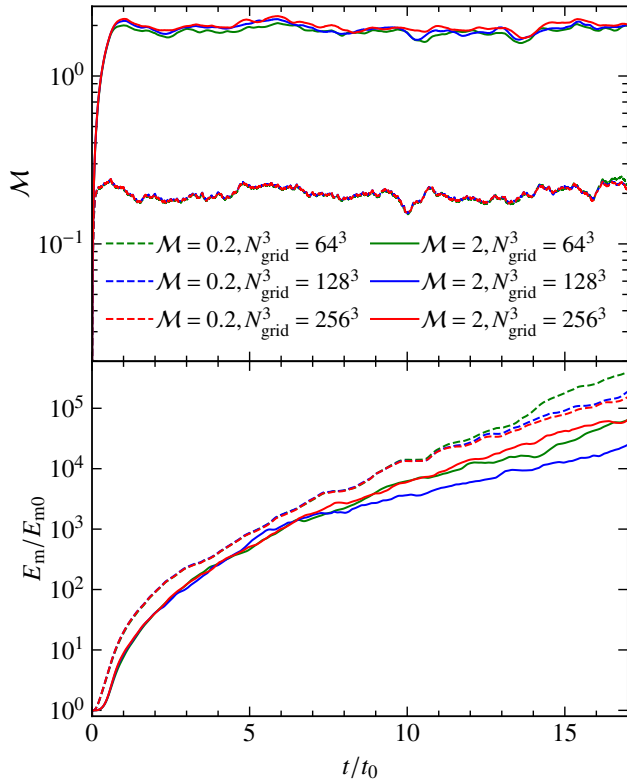


Figure A2. Same as Fig. A1, but for subsonic and supersonic weakly-collisional turbulent dynamo simulations with fixed $N_{\text{ppc}} = 100$ particles per cell and varying grid resolution of $N_{\text{grid}}^3 = 64^3, 128^3$ and 256^3 . The Mach number and growth rate are converged with $N_{\text{grid}}^3 = 128^3$ in both the subsonic and supersonic regimes.

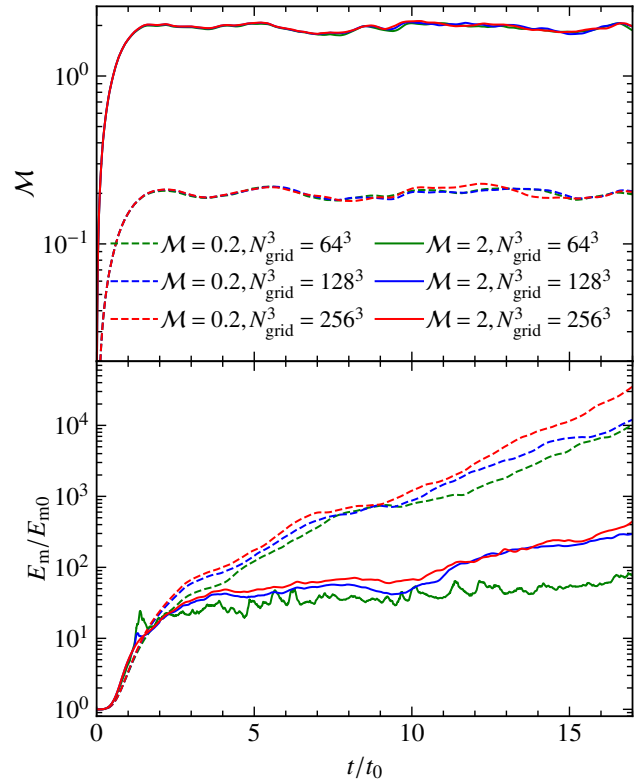


Figure B1. Same as Fig. A2, but for subsonic and supersonic MHD turbulent dynamo simulations with kinetic Reynolds number, $\text{Re} = 500$. The numerical simulations show convergence with $N_{\text{grid}}^3 = 128^3$.

APPENDIX B: GRID RESOLUTION CONVERGENCE TEST FOR MHD SIMULATIONS

To show the convergence of our subsonic and supersonic MHD simulations, we repeat our numerical experiments with varying grid resolution, $N_{\text{grid}}^3 = 64^3, 128^3$, and 256^3 . We find that the Mach number and magnetic energy growth rate are converged with $N_{\text{grid}}^3 = 128^3$ for both the $\mathcal{M} = 0.2$ and $\mathcal{M} = 2$ MHD simulations.

This paper has been typeset from a $\text{\TeX}/\text{\LaTeX}$ file prepared by the author.